How important is air-sea coupling in ENSO and MJO evolution?

Matthew Newman[1], Prashant D. Sardeshmukh[1], and Cécile Penland[2]

[1]CIRES Climate Diagnostics Center, University of Colorado, and Physical Sciences Division/NOAA Earth System Research Laboratory, Boulder, Colorado

[2]Physical Sciences Division/NOAA Earth System Research Laboratory, Boulder, Colorado

Email: matt.newman@noaa.gov

Submitted: Tuesday June 3, 2008
Revised: Thursday, December 11, 2008

Journal of Climate, in press

ABSTRACT

The effect of air-sea coupling on tropical climate variability is investigated in a coupled linear inverse model (LIM) derived from the simultaneous and 6-day lag covariances of observed 7-day running mean departures from the annual cycle. The model predicts the covariances at all other lags. The predicted and observed lag covariances, as well as the associated power spectra, are generally found to agree within sampling uncertainty. This validates the LIM's basic premise that beyond daily time scales, the evolution of tropical atmospheric and oceanic anomalies is effectively linear and stochastically driven. It also justifies a linear diagnosis of air-sea coupling in the system.

The results show that air-sea coupling has a very small effect on subseasonal atmospheric variability. It has much larger effects on longer-term variability, in both the atmosphere and ocean, including greatly increasing the amplitude of ENSO and lengthening its dominant period from two to four years. Consistent with these results, the eigenvectors of the system's dynamical evolution operator also separate into two distinct, but nonorthogonal, subspaces: one governing the nearly uncoupled subseasonal dynamics, and the other governing the strongly coupled longer term dynamics. These subspaces arise naturally from the LIM analysis; no bandpass frequency filtering is applied. One implication of this remarkably clean separation of the uncoupled and coupled dynamics is that GCM errors in anomalous tropical air-sea coupling may cause substantial errors on interannual and longer time scales, but probably not on the subseasonal scales associated with the MJO.

1. Introduction

Despite many years of coordinated model development in the climate research community, realistic simulations of tropical variability have remained elusive in coupled climate models, both on the interannual time scales of El Niño-Southern Oscillation (ENSO) and the subseasonal time scales of the Madden-Julian Oscillation (MJO). Figure 1 highlights one aspect of the difficulty for 18 global coupled models participating in Phase 3 of the World Climate Research Program's Coupled Model Intercomparison Project (CMIP-3), used in the Fourth Assessment Report (AR4) of the Intergovernmental Panel on Climate Change (IPCC, 2007). The model spectra of the leading principal component (PC) of monthly tropical SST variability during 1950-1999 show not only very different total power compared to the observed spectrum but also different timescales in which it is concentrated. In many cases they also appear more sharply peaked than the observed spectrum, which, apart from a rather broad peak at 4-yr periods, approximates the spectrum of red noise with an 8-month correlation scale. Such an observed spectrum is suggestive of a damped linear system with broadband stochastic forcing, i.e. forcing whose correlation scale is much shorter than 8 months.

One possible source of the climate model errors is the misrepresentation of shorter-term tropical variability (e.g., Fedorov et al. 2003), given some evidence that MJO episodes can initiate ENSO events (e.g., Kessler et al. 1995; McPhaden 1999; van Oldenborgh 2000; Bergman et al. 2001; Zhang and Gottschalck 2002; Zavala-Garay et al. 2005; Roundy and Kiladis 2006; McPhaden et al. 2006). Additionally, ENSO itself may modify MJO variability (e.g., Kessler 2001; Tam and Lau 2005; Pohl and Matthews 2007; Hendon et al. 2007). It is thus of concern that not only do GCMs continue to have

difficulty reproducing MJO phase speeds and vertical structures (e.g., Lin et al. 2004, 2006), but also that MJO simulations are particularly problematic in the western Pacific (e.g., Sperber et al. 2005; Zhang et al. 2006).

In searching for the causes of such model deficiencies, a key research issue is how air-sea coupling affects MJO and ENSO development. Although coupled theories of ENSO are very well established (e.g., Bjerknes 1969; Schopf and Suarez 1988; Battisti and Hirst 1989; Jin 1997; Wang et al. 1999), it is less clear how important coupling is to the initiation of ENSO events, and also precisely how it affects the overall stability of the system. How air-sea coupling influences the MJO is another unsettled question. Although SST anomalies of a few tenths of a degree are apparently induced by MJO winds and cloudiness that drive changes in surface heat and radiative fluxes (Shinoda et al. 1998; Woolnough et al. 2000), it is unclear how -- and how strongly -- those SST anomalies then feed back on the MJO. Studies with AGCMs coupled to an interactive ocean report conflicting results. Depending upon the model, coupling either causes the magnitude of intraseasonal variability to increase (Zheng et al. 2004) or to decrease (Inness and Slingo 2003; Pegion and Kirtman 2008) relative to uncoupled simulations. Some studies find that coupling leads to improved MJO simulations and/or forecasts (Zheng et al. 2004), but others do not (Hendon 2000; Liess et al. 2004; Lin et al. 2006).

To improve the tropical simulations of global coupled GCMs, one needs diagnostic methods that are equally applicable to observed and simulated climates. One useful approach has been to construct so-called “intermediate” coupled models that make key simplifying assumptions but still retain the important physics (e.g., Cane and Zebiak 1985; Battisti and Hirst 1989; Neelin and Jin 1993; Chang 1994; Jin 1997; Neelin and

Zeng 2000). We focus here on a different but complementary approach: to diagnose the impacts of air-sea coupling in an *empirically* determined dynamical model of the observed coupled system. Specifically, we construct a coupled linear inverse model (LIM), following procedures similar to those described in Penland and Sardeshmukh (1995; hereafter PS95), in which the dynamical evolution operator is estimated from the observed statistics of weekly-averaged tropical variations over the last 24 years. Evidence that such a LIM should be useful for our diagnostic purposes is provided in Fig. 1 by the favorable comparison of the LIM-predicted spectrum (along with confidence intervals, see section 3.3) of the leading PC of tropical SST with the corresponding observed and coupled GCM spectra. Our LIM diagnosis may not necessarily lead to the same kind of physical understanding as the intermediate coupled models, but because it simulates the observed variability just as well as -- or even better than -- many coupled GCMs, we believe it can provide a reliable quantification of the coupling effects.

Most previous LIMs were constructed using only atmospheric or only oceanic data. Atmospheric LIMs (A-LIMs; Penland and Ghil 1993; Winkler et al 2001, hereafter WNS; Newman et al 2003; Newman and Sardeshmukh 2008) for winter and summer seasons, based on weekly Northern Hemisphere streamfunction and tropical diabatic heating anomaly data, and oceanic LIMs (O-LIMs; Penland and Matrosova 1994; PS95; Penland 1996; Penland and Matrosova 1998; Johnson et al. 2000; Newman 2007; Alexander et al. 2008), based on seasonal or annual mean SST anomaly data, have both been shown to have forecast skill competitive with that of comprehensive nonlinear GCMs. Indeed Penland's O-LIM is currently used to make real-time SST forecasts that are included in NOAA's regular Climate Diagnostics Bulletin. Newman et al. (2003)

showed that their A-LIM's Week 2 tropical diabatic heating forecasts had comparable skill to that of a bias-corrected version of the GCM used operationally in 1998 at NCEP (Whitaker et al. 2003). Over the western Pacific, a potentially important region of air-sea coupling on subseasonal scales, the A-LIM's skill was considerably higher.

One can think of several ways to improve the A-LIMs and O-LIMs just mentioned. However, instead of doing this independently of each other, it is evident that much could be gained by coupling the two. From a forecasting standpoint alone, one can imagine how such a coupled LIM (C-LIM) might improve upon the skill of each. For example, equatorial heating anomalies at the dateline would evolve differently depending upon the SST conditions. If MJO propagation were significantly impacted by air/sea interactions, then the C-LIM would also be better at predicting the MJO than an A-LIM. Also, some of the unpredictable rapid variations treated as stochastic noise in the seasonal O-LIM may be associated with predictable atmospheric variations on weekly time scales, and may lead to improved SST prediction skill. Beyond improving forecasts of its component LIMs, however, a C-LIM would allow explicit separation of the "internal" oceanic and atmospheric dynamics from the coupled dynamics (see Newman et al. 2000 for an extratropical example).

The primary aim of this paper is to construct a C-LIM useful not only for simulating and predicting tropical anomalies on subseasonal to seasonal scales, but also for diagnosing the effects of air-sea coupling on tropical climate variability in a unified dynamical framework. Details of the C-LIM's construction, including the observational datasets employed, are discussed in section 2. In section 3, we show that coupling improves both atmospheric and SST forecast skill; that is, the C-LIM's forecast skill is as good as or

better than the A-LIM and O-LIM skill in their respective domains. As a further key demonstration of linear dynamics justifying our linear diagnosis here, we show that the C-LIM reproduces the observed lag-covariances at much longer lags than the 6-day lag at which it is trained, and also the power spectra of the leading PCs of both SST and diabatic heating variability. Section 4 presents a detailed diagnosis of the coupling impacts on both atmospheric and oceanic variability. The interpretation of that diagnosis is greatly clarified by a striking discovery of this paper: a sharp separation of the eigenvectors of the C-LIM's (and therefore presumably also the real tropical climate system's) dynamical evolution operator into two distinct sets, a set governing the nearly uncoupled subseasonal dynamics, and another governing the strongly coupled longer term dynamics. Section 5 present further results on how coupling impacts MJO and ENSO evolution, and concluding remarks are made in section 6.

2. Model details and data

Linear inverse modeling may be broadly defined as extracting the dynamical evolution operator $\mathbf{L}$ of the system

$$(1) \qquad \frac{d\mathbf{x}}{dt} = \mathbf{L}\mathbf{x} + \xi \ ,$$

from its observed statistics, as described for example in PS95 (see also Penland 1989, 1996; Penland and Ghil 1993; Delsole and Hou 1999; Winkler et al 2001; Newman et al 2003; Newman 2007; Alexander et al. 2008; Newman and Sardeshmukh 2008). The procedure and its strengths and pitfalls are discussed at length in these papers, so we will only provide its bare essentials here for convenience of later discussion.

In any multidimensional statistically stationary system with components x_i, one may define a time lag covariance matrix $\mathbf{C}(\tau)$ with elements $C_{ij}(\tau) = \langle x_i(t+\tau) x_j(t) \rangle$, where angle brackets denote a long-term average. In linear inverse modeling, one assumes that the system satisfies $\mathbf{C}(\tau) = \mathbf{G}(\tau)\mathbf{C}(0)$, where importantly $\mathbf{G}(\tau) = exp(\mathbf{L}\tau)$ and $\mathbf{L}$ is a constant matrix. One then uses this relationship to estimate $\mathbf{L}$ from observational estimates of $\mathbf{C}(0)$ and $\mathbf{C}(\tau_o)$ at some lag τ_o. In such a system any two states separated by a time interval τ are related as $\mathbf{x}(t+\tau) = \mathbf{G}(\tau)\mathbf{x}(t) + \varepsilon$, where ε is a random error vector with covariance $\mathbf{E}(\tau) = \mathbf{C}(0) - \mathbf{G}(\tau)\mathbf{C}(0)\mathbf{G}^T(\tau)$. Note that the system need not have Gaussian statistics for these relations to hold. However, for its statistics to be stationary, $\mathbf{L}$ must be dissipative, i.e. its eigenvalues must have negative real parts. In a forecasting context, $\mathbf{G}(\tau)\mathbf{x}(t)$ represents the "best" forecast (in a least squares sense) of $\mathbf{x}(t+\tau)$ given $\mathbf{x}(t)$, and $\mathbf{E}(\tau)$ represents the expected covariance of its error. Note that for large lead times τ, $\mathbf{G}(\tau)\mathbf{x}(t) \Rightarrow 0$ and $\mathbf{E}(\tau) \Rightarrow \mathbf{C}(0)$. Note also that unlike multiple linear regression, determination of $\mathbf{G}$ at one lag τ_o gives $\mathbf{G}$ at all other lags. One can also use the estimates of the forecast error covariance to estimate the statistics of the noise forcing ξ responsible for the forecast error ε.

For our C-LIM, we choose the model state vector $\mathbf{x}$ to be

$$\mathbf{x} = \begin{bmatrix} \mathbf{T}_o \\ \psi \\ \mathbf{H} \\ \chi \end{bmatrix}$$

where $\mathbf{T}_O$ is anomalous sea-surface temperature, ψ is anomalous streamfunction, $\mathbf{H}$ is anomalous diabatic heating, and χ is anomalous velocity potential. An atmospheric subvector is also defined as

$$\mathbf{x}_A = \begin{bmatrix} \psi \\ \mathbf{H} \\ \chi \end{bmatrix}.$$

All quantities represent 7-day running means. Rapid fluctuations in wind stress, heat flux, and other phenomena with correlation timescales much shorter than 7 days therefore constitute the noise term in (1). Twenty-four years (1982 to 2005) of data were used to define $\mathbf{x}$. The diabatic heating rates were determined from an improved iterative solution of the "chi-problem" (Sardeshmukh 1993; Sardeshmukh et al. 1999), as described in WNS. Weekly averaged SST data were obtained from the NCEP OI V2 dataset (Reynolds et al. 2002), and then interpolated to daily resolution. Anomalies were defined by removing the annual cycle from the 7-day running means, where the annual cycle was defined by running a 31-point smoother on the daily climatology of the lowpass data. Circulation anomalies (ψ and χ) were determined at 250, 550, and 850 hPa, and heating anomalies were determined at 400, 700, and 1000 hPa. All circulation variables were spectrally truncated to T21 and transformed onto a Gaussian grid; SST was area-averaged onto this same grid. Diabatic heating anomalies were further smoothed using a T21 spectral filter that attenuates small-scale features and Gibbs phenomena (Sardeshmukh and Hoskins 1984).

The filtered anomaly fields were then projected onto their leading Empirical Orthogonal Functions (EOFs), which were determined in the tropical belt 25°S—25°N. Prior to

computing the EOFs, each field was normalized by its climatological root-mean-square amplitude over the domain. The EOFs of streamfunction and velocity potential were each computed from a vector combining the normalized 850, 550, and 250 hPa anomalies, and the EOFs of heating from a vector combining the normalized 1000, 700, and 400 hPa anomalies, rather than at each level separately. The leading 20/7/17/3 EOFs of $\mathbf{T}_O/\psi/\mathbf{H}/\chi$ were retained, which explained about 76/44/36/67 percent of the variability of their respective fields. Locally, however, the amount of variance explained can be considerably higher (or lower), as seen in Fig. 2, which shows the (untruncated) variance of $\mathbf{T}_O$, $\mathbf{H}_{400}$ (that is, **H** at 400 hPa), ψ_{250} and χ_{250} (that is, ψ and χ at 250 hPa), and the local fraction of variance retained by the truncated EOF basis for each field.

The time-varying coefficients of these EOFs, i.e., the principal components (PCs), define the 47-component state vector **x**. A training lag of τ_o=6 d was used to determine **L**. The EOF truncations and training lag were chosen to maximize the LIM's cross-validated forecast skill while avoiding some sampling problems (see below and WNS), but otherwise do not qualitatively affect any of the points made in this paper. In particular, retaining more EOFs and thus more variance did not result in significant and unambiguous improvements in the metrics considered in the next section, nor was the estimate of the impact of coupling materially altered. Moreover, retaining several less $\mathbf{T}_O$ and $\mathbf{H}_{400}$ EOFs also gave similar results except over the Indian ocean region. We also constructed a corresponding A-LIM (O-LIM) using the same atmospheric (SST) truncation, so that $\mathbf{x}_A$ ($\mathbf{T}_O$) was represented by a 27-component (20-component) state vector.

For use in a calculation regarding MJO evolution, we also constructed a "highpass" filtered dataset by subtracting the centered 49-day mean from each day. Highpass EOFs and PCs were then determined from the *combined* data vector, rather than determining EOFs for each variable separately as in constructing the LIM. The resulting leading two PCs (not shown), although not based on meridionally-averaged data as in Wheeler and Hendon (2004), strongly correspond to (i.e., are highly correlated with) their Realtime Multivariate MJO series 1 (RMM1) and 2 (RMM2). Highpass $\mathbf{T}_o$, $\mathbf{H}_{400}$, and 850 hPa winds regressed on PC1 and PC2 are shown in Fig. 3; note that these fields are not truncated in the EOF space used for the LIM. Although these regressed fields are based on a relatively crude 14-98 day bandpass filter, they are quite similar to composites of 20-100 day bandpass-filtered precipitation, SST, and surface wind anomalies associated with greater than one-sigma excursions of RMM1 and RMM2 (Waliser et al. 2008), except that our spatial smoothing and regression approach yields somewhat reduced amplitudes.

3. Evaluating the LIM

3.1. Forecast skill

We first investigate whether including both atmospheric and oceanic components in the state vector improves LIM forecast skill, by comparing the C-LIM's skill to either O-LIM or A-LIM skill alone. As described in WNS, all estimates of forecast skill were determined by comparing cross-validated (i.e. verified on independent data) model predictions to the *untruncated* data.

Figure 3 shows that the C-LIM does have higher $\mathbf{H}_{400}$ forecast skill, measured by local anomaly correlation, at forecast leads of 28 (Figs. 4a and b) and 150 (Figs. 4c and d)

days. In general, the C-LIM's atmospheric forecast skill improvement is larger for longer lead times, for all variables at all levels (not shown). This enhancement is basically due to the C-LIM's ability to capture some aspects of the slow $\mathbf{T}_O$ evolution. In fact, a second set of C-LIM forecasts in which $\mathbf{T}_O$ is held fixed (i.e., $\mathbf{T}_O(t) = \mathbf{T}_O(0)$) has much lower 150-day forecast skill (not shown). $\mathbf{T}_O$ evolution is not so important at the shorter 28-day lead, at which the fixed $\mathbf{T}_O$ forecasts have about the same forecast skill as the C-LIM.

The fact that the C-LIM's skill is only slightly higher than the A-LIM's at Day 28 does not necessarily imply that SST impacts are small over this range, because the A-LIM also implicitly includes linear diagnostic relationships between $\mathbf{x}_A$ and $\mathbf{T}_O$. The true impact of $\mathbf{T}_O$ on the atmospheric Day 28 forecasts is demonstrated by comparing C-LIM forecasts in which only $\mathbf{x}_A$ is initialized (i.e., $\mathbf{T}_O(t=0) = 0$) with the full C-LIM forecasts. The resulting $\mathbf{H}_{400}$ forecast skill is significantly degraded (Figs. 4e and 4f), suggesting that initial SST conditions impact western Pacific atmospheric skill even at leads as short as 28 days. On the other hand, for shorter forecast leads (such as 14 days; not shown), a similar analysis shows that atmospheric skill over the equatorial Indian and west Pacific Oceans is considerably more independent of $\mathbf{T}_O$.

Including $\mathbf{x}_A$ in $\mathbf{x}$ improves $\mathbf{T}_O$ forecast skill but in a fairly minor way, for example at 150-day (Figs. 5a and c) and 270-day (Figs. 5b and d) forecast lead times. This improvement is not merely due to the higher order of the C-LIM state vector, since O-LIM forecasts are not improved further with a higher order state vector. Neither does the improved skill appear to be due to initial atmospheric conditions, since even C-LIM forecasts initialized with $\mathbf{x}_A(t=0) = 0$ (Figs. 5e and f) are slightly more skillful than the O-LIM. One possibility is that small sampling errors are introduced in the O-LIM operator

when the atmospheric state is not explicitly part of the state vector. Of course, these skill differences are so small that they may also be simply due to chance.

3.2. Lag-covariability in observations and the LIM

A key test of the LIM is to determine how well it approximates observed lag-covariability at lags other than the lag on which it is trained. This "tau-test" (Penland 1989; PS95) can take many forms, but one of the more easily interpretable is to recall that (1) immediately implies that $\mathbf{C}(\tau) = \mathbf{G}(\tau)\ \mathbf{C}(0)$, where $\mathbf{G}(\tau) = \exp(\mathbf{L}\tau)$. That is, the LIM should be able to reproduce observed lag-covariance statistics at all lags. For example, Newman and Sardeshmukh (2008) showed their LIM of extratropical anomalies reproduced the observed 21-day lag-autocovariances of streamfunction and sea level pressure. We employ a similar test here for diabatic heating and SST.

Figure 6 compares the observed and predicted lag-autocovariances of $\mathbf{H}_{400}$ and $\mathbf{T}_O$. The C-LIM's prediction of 28-day lag-autocovariance of $\mathbf{H}_{400}$ (Figs. 6a and b) is significantly better than that of the A-LIM (not shown) and compares well with observations. We find that the small differences between the two fields over the central and eastern Pacific are largely a consequence of the reduced variance represented by the **H** EOF truncation (Fig. 2), whereas the differences in the western Pacific are not. Similar comparisons exist at other levels and for χ and ψ.

The C-LIM's predicted 150-day lag-autocovariance of $\mathbf{T}_O$ (Figs. 6c and d) also compares very well with observations, with relatively minor differences well within sampling uncertainty. However, for the longer lag of 270 days (Figs. 6e and f), while the C-LIM

prediction of the lag-autocovariance has about the right magnitude, it has only a hint of the pronounced local minimum centered at about 130°W.

3.3. Power spectra

A complementary test of linearity is to make a more direct comparison of the C-LIM's predicted low-frequency variance with observations by either computing the power in desired frequency bands directly from (1) (as in Penland and Ghil 1993), or by making a long run of (1) and collecting statistics. We followed the latter approach, integrating (1) for 2400 years using the method described in Penland and Matrosova (1994). The white noise forcing $\xi = \sum_j \mathbf{q}_j \eta_j r_j(t)$ was specified using independent Gaussian white noises $r_j(t)$ with unit variance, where $\mathbf{q}_j$ and $(\eta_j)^2$ as the eigenvectors and eigenvalues, respectively, of the positive-definite noise covariance matrix $\mathbf{Q} = \langle \xi \xi^T \rangle dt$ determined as a residual in the Fluctuation-Dissipation relationship

$$(2) \qquad d\mathbf{C}(0)/dt = \mathbf{0} = \mathbf{L}\mathbf{C}(0) + \mathbf{C}(0)\mathbf{L}^T + \mathbf{Q} ,$$

given the observed $\mathbf{C}(0)$ and $\mathbf{L}$. The resulting $\mathbf{Q}$ is a legitimate covariance matrix since all its eigenvalues were found to be positive. The 2400-yr model time series was separated into 100 24-yr segments. The observed spectra and the ensemble mean of model spectra for the three leading PCs of $\mathbf{T}_O$ and $\mathbf{H}$ are shown in Figs. 7 and 8, respectively. The corresponding EOF pattern for each spectrum is shown in the inset panels. The gray shading shows the 95% confidence intervals of these spectra, estimated using the 100 model realizations.

The LIM reproduces the main features of the observed spectrum of the leading PC of each variable (top panels of Figs. 7 and 8; results for ψ and χ are not shown). Obviously, the mean LIM spectra are much smoother than observed, due to the relatively few degrees of freedom in the truncated EOF space. On the other hand, the irregularity of the observed spectra is at least partly due to sampling, as indicated by the confidence intervals that show how much variation in the spectra could occur simply from different realizations.

For the higher order PCs, the LIM reproduces the intraseasonal peak centered at a period of about 50 days (Fig. 8), but on longer time scales the LIM appears to underestimate the period of a quasi-decadal spectral peak for both the atmospheric and $\mathbf{T}_O$ PCs. Comparing the top panel to the bottom two panels in Fig. 7 also suggests that the difference between the observed and LIM-predicted 270-day lag-covariance (Figs. 6e and f) is due to discrepancies in the slow evolution of the higher order $\mathbf{T}_O$/PCs but not in the time series of the main ENSO pattern (i.e., $\mathbf{T}_O$/PC1) itself. Of course, given the short data record there is considerable uncertainty in the observational spectra on these longest time scales as well.

4. Effects of air-sea coupling

4.1. Decoupling the linear dynamical operator

The effects of coupling between the atmosphere and ocean may be investigated in a framework in which (1) is rewritten as

$$\frac{d}{dt}\begin{bmatrix}\mathbf{T}_O\\ \mathbf{x}_A\end{bmatrix}=\begin{bmatrix}\mathbf{L}_{OO} & \mathbf{L}_{OA}\\ \mathbf{L}_{AO} & \mathbf{L}_{AA}\end{bmatrix}\begin{bmatrix}\mathbf{T}_O\\ \mathbf{x}_A\end{bmatrix}+\begin{bmatrix}\xi_O\\ \xi_A\end{bmatrix}. \tag{3}$$

Note that $\mathbf{L}_{AA}$ is distinct from the linear operator obtained from the A-LIM of $\mathbf{x}_A$ alone. Recall from the discussion of the A-LIM's forecast skill (Fig. 4) that it implicitly includes linear diagnostic relationships between $\mathbf{x}_A$ and $\mathbf{T}_O$. By explicitly separating out the effects of $\mathbf{T}_O$ on $\mathbf{x}_A$ and vice versa, (3) enables us to identify $\mathbf{L}_{AA}$ more cleanly with the "internal" (i.e., uncoupled) atmospheric dynamics. This is also the case when comparing $\mathbf{L}_{OO}$ to the O-LIM. Of course, $\mathbf{L}_{AA}$ and $\mathbf{L}_{OO}$ may each implicitly retain the influence of variables not included in $\mathbf{x}$, and to the extent that both terms are related to the *same* unspecified variables they may not be entirely independent.

We define a new "uncoupled" operator $\mathbf{L}_{unc}$ in which $\mathbf{L}_{AO} = \mathbf{L}_{OA} = 0$, resulting in the two independent dynamical systems,

$$\frac{d\mathbf{x}_A}{dt} = \mathbf{L}_{AA}\mathbf{x}_A + \boldsymbol{\xi}_A \tag{4}$$

and

$$\frac{d\mathbf{T}_O}{dt} = \mathbf{L}_{OO}\mathbf{T}_O + \boldsymbol{\xi}_O . \tag{5}$$

The atmospheric and SST noises are uncorrelated with each other but are otherwise unchanged from the full LIM calculation above. We made a second 2400 yr run using this uncoupled model. The resulting spectra (green lines in Figs. 7 and 8) make clear that without coupling $\mathbf{T}_O$/PC1 variability is very weak and shifts to a shorter, two-year period. The impact of coupling is greatest for this PC; overall, uncoupling reduces total $\mathbf{T}_O$ variance by a little over two-thirds in the Pacific and by roughly a third in the Atlantic (not shown). In addition, the meridional width of the region of large SST variability is somewhat reduced in the uncoupled run (not shown). Unsurprisingly, interannual

atmospheric variability is virtually eliminated (Fig. 8). On the other hand, intraseasonal atmospheric variability is mostly unchanged: there is essentially no difference between the full and uncoupled LIM atmospheric PC spectra for periods of less than about 50 days, with about a 10% reduction for longer-period variability over the Indian Ocean.

4.2. Coupled and nearly uncoupled subspaces of L

We next show how the eigenmodes of $\mathbf{L}$ (also sometimes called principal oscillation patterns, or POPs; Hasselmann 1988; von Storch et al. 1988; Penland 1989), obtained from $\mathbf{L}\mathbf{u}_j = \mathbf{u}_j\,\omega_j$ where $\mathbf{u}_j$ are the eigenmodes and ω_j the corresponding complex eigenvalues, naturally form two distinct subspaces that can be used to distinguish between coupled and uncoupled dynamics in this system. Fig. 9a shows the eigenvalues, plotted as frequency, $\mathrm{Im}(\omega_j/2\pi)$, vs. e-folding time (eft), $-\mathrm{Re}(\omega_j)^{-1}$. The eigenmodes fall into two distinct classes: one class has large amplitude in both $\mathbf{T}_\mathrm{O}$ and $\mathbf{x}_\mathrm{A}$ ("coupled" eigenmodes $\mathbf{u}_j^{\mathrm{coup}}$) and the other class has large amplitude in $\mathbf{x}_\mathrm{A}$ but small amplitude in $\mathbf{T}_\mathrm{O}$ (nearly uncoupled or "internal atmospheric" eigenmodes $\mathbf{u}_j^{\mathrm{int}}$). Note from Fig. 9a that $\mathbf{u}_j^{\mathrm{coup}}$ also have relatively low frequency and large efts, while $\mathbf{u}_j^{\mathrm{int}}$ have relatively high frequency and small efts. Also shown in Fig. 9a are the eigenvalues of $\mathbf{L}_{\mathrm{unc}}$, whose eigenmodes also fall into two distinct classes, but now by construction: one class has amplitude in $\mathbf{T}_\mathrm{O}$ but zero amplitude in $\mathbf{x}_\mathrm{A}$ ("SST-only" modes), and the other class has amplitude in $\mathbf{x}_\mathrm{A}$ but zero amplitude in $\mathbf{T}_\mathrm{O}$ ("atmosphere-only" modes). We find a strikingly close correspondence between $\mathbf{u}_j^{\mathrm{int}}$ and the atmosphere-only eigenmodes of $\mathbf{L}_{\mathrm{unc}}$, not only because most of the corresponding eigenvalues have such minor differences but also because the eigenmodes themselves are mostly so similar. This latter

point is clear from Fig. 9b, which shows the maximum pattern correlations (Borges and Sardeshmukh 1995) between the closest corresponding eigenmodes of $\mathbf{L}$ and $\mathbf{L}_{\mathrm{unc}}$. Only the lowest frequency $\mathbf{u}_j^{\mathrm{int}}$ have structures with even minor differences from their uncoupled atmosphere-only counterparts. On the other hand, relatively little correspondence exists between the $\mathbf{u}_j^{\mathrm{coup}}$ and the SST-only eigenmodes of $\mathbf{L}_{\mathrm{unc}}$.

Figure 9 strongly suggests that while air-sea coupling greatly modifies the slow SST eigenmode subspace, it only minimally modifies the faster internal atmospheric eigenmode subspace. For example, a comparison of the two leading propagating eigenmodes of $\mathbf{L}$ and $\mathbf{L}_{\mathrm{unc}}$ (Fig. 10) shows that the least damped eigenmode of $\mathbf{L}$ has an ENSO-like pattern and period entirely absent in the uncoupled SST-only eigenmodes. In contrast, the least damped internal atmospheric eigenmode (Fig. 11), with period and pattern characteristic of an MJO, is virtually identical to the least damped atmosphere-only eigenmode. For the few internal atmospheric eigenmodes that are altered by coupling, the differences between eigenmode structures are fairly subtle, and because they are strongly damped, even relatively large changes in period have a minor impact on their evolution.

Since the subspace defined by the internal atmospheric eigenmodes of the full operator corresponds so well to the subspace defined by the atmosphere-only eigenmodes of the uncoupled operator, it likely represents that portion of the atmospheric dynamics only weakly coupled (if at all) to SST. This suggests that coupled and internal atmospheric variability can be naturally separated by dividing the state vector $\mathbf{x}$ into two parts, $\mathbf{x} = \mathbf{x}^{\mathrm{coup}} + \mathbf{x}^{\mathrm{int}}$, where

$$\mathbf{x}^{\text{coup}} = \sum_j \mathbf{u}_j^{\text{coup}} \alpha_j^{\text{coup}}(t),$$

and

$$\mathbf{x}^{\text{int}} = \sum_j \mathbf{u}_j^{\text{int}} \alpha_j^{\text{int}}(t),$$

an approach analogous to the nonnormal filter used by Penland and Matrosova (2006) to isolate ENSO. The time series $\alpha_j^{\text{int}}(t)$ and $\alpha_j^{\text{coup}}(t)$ are determined by taking the inner product of **x**(t) with the corresponding (biorthogonal) adjoint vectors. Note that **L** is not self-adjoint and these two subspaces are not orthogonal. That is, the total variance of **x** is *not* the sum of the variances of $\mathbf{x}^{\text{coup}}$ and $\mathbf{x}^{\text{int}}$. However, in the absence of forcing (including stochastic forcing), $\mathbf{x}^{\text{coup}}$ and $\mathbf{x}^{\text{int}}$ do not interact: they evolve independently of each other.

The spectra of the leading **H** PCs projected in these two subspaces, $\mathbf{H}^{\text{coup}}$ and $\mathbf{H}^{\text{int}}$, are shown in Fig. 8. For **H**/PC1 the separation is particularly distinct: $\mathbf{H}^{\text{coup}}$/PC1 approximates the spectrum of red noise with about an 8-month correlation scale and represents almost all the **H**/PC1 interannual variability, while $\mathbf{H}^{\text{int}}$/PC1 approximates the spectrum of red noise with about an 8-day correlation scale and represents almost all the **H**/PC1 intraseasonal variability. While the spectral tails of the two processes overlap for variability within the intra-annual band (periods of several months), separation into these coupled and internal atmospheric subspaces also acts, in effect, as a bandpass filter; that is, the sum of the $\mathbf{H}^{\text{coup}}$/PC1 spectrum and the $\mathbf{H}^{\text{int}}$/PC1 spectrum roughly equals the total

H/PC1 spectrum. A similar result exists for **H**/PC3, although its interannual variability is relatively much weaker.

For **H**/PC2, however, in the intra-annual band the two subspaces have substantial spectral overlap but in this case their variances are not additive. This means that **H**/PC2 variability in this frequency band projects on nonorthogonal eigenmodes (i.e., similar spatial structures but very different eigenvalues) in both subspaces. As a consequence, a bandpass filter of H/PC2 would confuse variability due to faster, largely uncoupled dynamics with variability due to slower, coupled dynamics.

5. Impact of coupling on the evolution of the MJO and ENSO

Having demonstrated how coupling affects the overall statistics of tropical variability, we next examine how coupling more specifically affects MJO and ENSO evolution, by integrating (1) forward from some suitable initial conditions. The evolution discussed below is entirely deterministic; that is, unlike the model runs discussed in the previous sections, no stochastic noise forcing is included in these integrations.

5.1. Evolution of the MJO

Figure 12 shows an example of MJO evolution in the C-LIM, initialized with a state obtained by regression on highpass PC2 (Fig. 12a; the same as Fig. 3b apart from relatively minor differences due to the EOF truncation). Note that although this "1-sigma event" initial condition is determined from the highpass dataset, its subsequent evolution is based upon the full C-LIM constructed from the 7-day running means.

After about two weeks (Fig. 12b), the state vector evolves into a pattern very similar to EOF1 of the highpass data (cf. Fig. 3a). [Conversely, a C-LIM integration initialized with

fields regressed on highpass PC1 evolves into highpass EOF2 (not shown).] Hovmuller diagrams of $\mathbf{H}_{400}$ and $\mathbf{T}_O$ averaged between 2^0S-2^0N (Fig. 12c) and ψ_{850} and χ_{850} at 8^0N (Fig. 12d) show continuous eastward phase propagation with a peak-to-peak period of roughly 50 days. Also, the vertical structure of **H** is "top-heavy" and tilted westward with height (not shown), with maxima about twice as strong and about 7^0 westward at 400 hPa compared to 700 hPa, which are both in agreement with Lin et al. (2004). These effects are weaker for maritime continent anomalies. The C-LIM also captures the not-entirely-smooth propagation of the anomaly, including the "jump" of convection across the maritime continent (e.g., Knutson and Weickmann 1987). Over one half cycle, peak amplitude decays by about two thirds, at about the decay rate of the leading internal atmospheric eigenmode (Fig. 11), reflecting the loss of MJO predictability in the presence of noise. As the atmospheric anomaly moves near the dateline, it induces an equatorial SST anomaly (Fig. 12b) propagating eastward at about 2.5 m/s (Fig. 12c), slower than the MJO but consistent with observed mid-Pacific oceanic Kelvin waves (e.g., Roundy and Kiladis 2006). Throughout the Tropics, $\mathbf{T}_O$ anomalies driven by the MJO in the C-LIM are fairly weak, on the order of 0.1 K, but are consistent in both pattern and amplitude with the regression results (Fig. 3) as well as with previous studies (e.g., Shinoda et al. 1998; Woolnough et al. 2000; Pegion and Kirtman 2008; Waliser et al. 2008).

When the same initial conditions are integrated forward using the uncoupled operator $\mathbf{L}_{unc}$ (Figs. 12e and f), the MJO evolution is largely unchanged, as might have been anticipated from section 4. Moreover, the MJO evolution occurs almost entirely within

the $\mathbf{x}^{int}$ subspace (not shown). Of special note is that even the uncoupled MJO propagates realistically through the western Pacific, in stark contrast to most GCM simulations.

Removing all interactions between **H** and other variables impacts MJO evolution much more significantly. We constructed a new operator ($\mathbf{L}_{adiabatic}$) in which ψ and χ still interact with each other and with $\mathbf{T}_O$ but internal atmospheric dynamics are otherwise adiabatic. The evolving anomaly (not shown) retains many MJO characteristics, but propagates about one third faster across the tropical Indo-Pacific and decays by about 95% over one half cycle. Interestingly, in the vicinity of South America the propagation speed is unaltered, consistent with primarily adiabatic dynamics in this region and/or the continued presence in the modified operator of implicit effects from some variable(s) not included in **x** (for example, interactions with land and/or the extratropics).

5.2. Optimal evolution of ENSO in the LIM

PS95 showed that the "optimal" initial condition for maximum amplification of tropical SST anomalies, obtained via a singular vector decomposition (SVD) of the system propagator $\mathbf{G}(\tau)$ under the domain-integrated (L2) norm of $\mathbf{T}_O$ (e.g., Farrell 1988; PS95; WNS), is also the most relevant initial condition for ENSO development. The SVD analysis yields a dominant pair $\mathbf{e}_1,\mathbf{f}_1$ of normalized singular vectors and maximum singular value λ_1, such that the initial condition $\mathbf{f}_1$ at time t leads to the anomaly $\mathbf{G}\ \mathbf{f}_1 = \lambda_1\mathbf{e}_1$ at later time $t + \tau$. The maximum possible anomaly growth factor during the time interval τ, $\lambda_1^2(\tau)$, is sometimes called the "maximum amplification" (MA) curve (PS95), which peaks here at τ_{max}~150 d (not shown).

We initialized a LIM run with the optimal initial condition for growth over a $\tau = \tau_{max}$ interval, shown in Fig. 13a; note its virtually zero initial atmospheric anomaly. The choice of τ is not too important, since for any $\tau > 28$ d the initial condition (and subsequent evolution over the next 210 days) is almost independent of τ. Our singular vector analysis produces results broadly similar to earlier studies using 3-month running mean data since 1950 (see, for example, PS95), with two main exceptions: our τ_{max} is shorter than in other studies, which found $\tau_{max} \sim 8$ months, and the optimal SST anomaly is of the same sign all along the equator, whereas other studies found a weak opposite-sign equatorial anomaly at about 140^0W. The former difference appears due to our use of weekly instead of seasonal data. The latter difference occurs for both weekly and seasonal LIMs, however, and is likely a consequence of our post-1982 data record.

Tropical evolution over the next 210 days, shown in Figs. 13b-e, can be roughly divided into three phases: about two months of transient development, then about three months of stationary development, followed finally by the anomaly's weakening. The first phase starts with a low-level equatorial westerly wind anomaly forming rapidly at the western edge (~160^0E) of the positive SST anomaly oriented northeastwards from the equator (Fig. 13a), reminiscent of the surface winds/SST pattern of the Pacific meridional mode (MM) (Vimont et al. 2003; Chang et al. 2007). A positive diabatic heating anomaly then also forms north of the equator (Fig. 13b), with negative anomaly over Indonesia. While the MM SST anomaly weakens, the equatorial $\mathbf{T}_O$ anomaly strengthens and this atmospheric anomaly slowly shifts eastward and southward onto the equator. Most of the amplification in this phase appears related to the MM SST anomaly and the opposite-signed SST anomaly to its west, a point confirmed by repeating the integration but

initializing with only the western Pacific/Indian Ocean SST anomaly (not shown). Then, during the second phase, quasi-stationary atmospheric and SST anomalies centered on the equator continue to amplify, apart from some minor variations due to the continuing eastward propagation of the steadily decaying MJO. Finally, the SST anomaly decays, although the heating anomaly near the dateline does not reach its peak for another few weeks, consistent with observations.

The picture is slightly complicated by the simultaneous excitation of an eastward propagating MJO (cf. Figs. 13d and e to Figs. 12c and d) by the initial condition. However, this MJO only minimally contributes to SST anomaly amplification, as can be seen by the evolution of the coupled modes alone (i.e., $\mathbf{x}^{\mathrm{coup}}(t)$) shown in Fig. 13f. This is entirely consistent with the existence of the non-orthogonal coupled and uncoupled subspaces demonstrated earlier. In other words, the same initial condition projects onto structures favorable for both ENSO and MJO evolution.

6. Summary and conclusion

To investigate the effect of air-sea coupling on the variability of weekly-averaged tropical anomalies, we have constructed a coupled LIM using the observed zero-lag and 6-day lag covariances of tropical SST and atmospheric variables. The model predicts the covariances at all other lags, and hence also the corresponding power spectra. The predicted and observed spectra and lag-covariances are generally found to be in agreement, even at much longer lags, at least up to the time interval associated with the maximum possible predictable growth of anomalous SST in the system. Such agreements validate the LIM's basic premise that the dynamics of tropical weekly averages are

effectively linear and stochastically driven, and justifies our linear diagnosis of the system.

We find that while anomalous air-sea coupling greatly increases interannual SST variability and lengthens the period of ENSO, it has a very small effect on intraseasonal atmospheric variability. Further analysis of the linear dynamical operator shows that coupling minimally modifies the fast atmospheric eigenmode subspace but greatly modifies the slower SST eigenmode subspace (the latter point echoing theoretical nonlinear modeling results such as those of Neelin and Jin 1993). Moreover, the sharp distinction between the two subspaces suggests that scale interactions between ENSO and MJO phenomena are relatively weak. Note that our analysis cannot rule out the possibility that coupling affects the stochastic forcing; that is, coupling effects on time scales much shorter than a week, including diurnal effects, may still exist.

The *predictable* evolution of ENSO apparently does not involve MJO forcing. This does not mean that the MJO has no effect on ENSO, since the optimal initial structure for ENSO could be excited by a series of MJO-like events similar to Fig. 12, as suggested for example by Zavala-Garay et al (2005). Additionally, extratropical noise could excite the meridional mode portion of the optimal structure, consistent with the "seasonal footprinting" mechanism (Vimont et al. 2003). However, since in either case these individual noise events would be largely unpredictable, it would not be until the SST anomaly pattern approximates that shown in Fig. 13a that ENSO begins to develop in a largely predictable manner.

Our study is clearly limited by the relatively short available data record of weekly SST. This has likely affected our estimate of the optimal structure, and perhaps also our predicted lag-covariances at very long lags (e.g., 270 days) as well as our spectral estimates for the higher order PCs at ultra-low frequencies. These are typically better simulated in O-LIMs constructed from much longer datasets, albeit from seasonal or yearly averages. Another obvious problem is that the "ocean" part of our state vector is SST alone. Including 20^0C isotherm depth in a LIM constructed from seasonal means (Newman et al 2008, in preparation) notably improves both SST forecasts and predicted lag-covariances over lags greater than about nine months, although its impact on shorter lags is small. It has also been suggested that the relationship between the MJO and oceanic Kelvin waves may appear more clearly in other ocean variables such as dynamic height (Roundy and Kiladis 2006), so our version of the C-LIM may be missing some dynamics on much shorter time scales as well. To completely diagnose ocean-atmosphere coupling, explicit subsurface information appears essential, but unfortunately the availability of such data on weekly time scales is currently limited. It is of course quite possible that some LIM deficiencies are not only due to data limitations but also to some nonlinear aspect of the coupled dynamics not treatable as linear terms plus stochastic noise, or to non-stationarity in the data (for example, a trend in the warm pool SSTs). Additionally, the impact of the EOF truncation may result in an underestimation of linear coupled processes for infrequent and/or high amplitude events. Still, keeping in mind that the LIM captures the observed spectral peaks better than many coupled GCMS, these deficiencies appear to represent a relatively small part of the variance and would require a correspondingly small modification of our conclusions.

Another limitation may be our assumption that **L** is independent of season. For three-month running mean SST anomalies, PS95 suggested that both the observed seasonality of SST variability and the tendency of ENSO to be phase-locked to the seasonal cycle might be explained with a fixed **L** but seasonal variation of both **Q** and the optimal structure (see also Penland 1996; for an opposing view, see Thompson and Battisti 2000). We likewise find that the initial conditions correspond best to the optimal pattern during spring (not shown), a result also consistent with the seasonal footprinting mechanism (Vimont et al. 2003; Chang et al. 2007). However, perhaps on weekly time scales the seasonality of **L** matters to the coupled climate system, given fundamental differences between summer and winter monsoons and the apparent seasonal dependence of MJO-ENSO interactions (Hendon et al 2007). We attempted to address this issue by constructing separate C-LIMs for the extended winter (November 1-March 31) and extended summer (April 1-October 31) seasons. These seasonally adjusted **L** operators gave modestly better results than the fixed **L** operator on shorter time scales. However, perhaps due to the limited length of the data set, the separate winter and summer C-LIMs were much *less* accurate on longer ENSO time scales. We suspect that seasonality is important, but that to construct a seasonally-varying LIM generally superior to the year-round LIM requires either more training data or else another approach to computing a cyclo-stationary LIM (e.g., Ortiz-Bevía 1997), both of which we defer to future research. We stress that none of the seasonality differences we did find materially altered our key conclusions concerning the relative importance of coupling at interannual vs. intraseasonal time scales.

Our results support the view that the MJO is fundamentally an atmospheric phenomenon with strong coupling between the circulation and deep convection, but minimal coupling to the underlying SST anomalies. The fact that diabatic heating has a much larger impact on the MJO in the C-LIM than air-sea coupling suggests that improving MJO simulations in AGCMs may depend much more on improving simulation of clouds and convective processes (e.g., Maloney and Hartman 2001; Zhang and Mu 2005; Lin et al. 2004, 2006; Vitart et al. 2007; Mu and Zhang 2008) than on merely coupling an AGCM to an OGCM or some other interactive ocean model.

Why then, do many (although not all) studies report improved MJO simulations in a coupled GCM than in the corresponding AGCM? One possibility is that such a result says more about the models than about nature. Perhaps improved MJO simulations in coupled GCMs result when one model error, say incorrect atmospheric physics, is compensated for by a second error, say incorrect coupling based upon incorrect local air-sea relationships (e.g., Wu et al 2006; Pegion and Kirtman 2008). Moreover, introducing coupling generally modifies the model climatology (e.g., Inness and Slingo 2003; Inness et al. 2003; Sperber et al. 2005; Zhang et al. 2006; Pegion and Kirtman 2008), potentially a more important factor than feedback from intraseasonal SST anomalies, especially in the far west Pacific where many models have mean surface easterlies instead of westerlies. Whether coupling likewise modifies the mean climate drift of model forecasts is also unclear. Note that our study does not address how coupling impacts the *mean* climate, since by construction there is no error in the C-LIM mean climate and no climate drift for forecasts at any lead time. Finally, it seems likely that coupling is a more complex process than is commonly assumed in simpler theoretical studies. Certainly, the

SST pattern associated with the MJO (e.g., Fig. 12a) is not simply a phase-shifted version of the atmospheric anomaly, so changes in surface fluxes due to remote SST anomalies and their influence on surface winds may be different from – and even partly oppose – changes due to local SST anomalies.

In this study, rather than distinguishing a priori between interannual and intraseasonal variability through filtering in pre-specified frequency bands, we let the dynamical system operator $\mathbf{L}$ make this distinction a posteriori through its coupled and internal atmospheric subspaces. This dynamically-based separation suggests that the more common frequency filter approach may mix different dynamical processes, represented in $\mathbf{L}$ by different nonnormal eigenmodes. While standard definitions of the MJO cleanly remove the mature ENSO phase (i.e., **H**/EOF1; Fig. 8), they may still retain the high-frequency tail of interannual variability (e.g., periods under about one year for **H**/EOF2) driven by coupled dynamics and consequently also retain a certain ambiguity when applied to both observational and model diagnosis. For example, introducing coupling in a GCM might improve forecasts of some MJO metric due to an improvement in the dynamics of ENSO, such as during potential onset phases, and not necessarily the dynamics of the MJO.

Finally, our uncoupled and adiabatic operators may be regarded as extreme examples of erroneous coupling in climate models. In the C-LIM, removing air-sea coupling leads to an ENSO whose period is too short and whose maximum amplitude is too far west, and removing coupling between the atmospheric circulation and diabatic heating results in an MJO that propagates and decays too rapidly. Both of these are common CGCM failings,

suggesting that the approach we have used in this paper might also be useful for diagnosing errors in comprehensive coupled climate models.

7. Acknowledgments

The authors thank George Kiladis and Klaus Weickmann for useful conversations. Ludmila Matrosova kindly supplied code to interpolate weekly SST to daily time scales. Paul Roundy and an anonymous reviewer made useful comments on an earlier version of the manuscript. We acknowledge the international modeling groups for providing their data for analysis, and the Program for Climate Model Diagnosis and Intercomparison (PCMDI) for collecting and archiving the model data. The IPCC Data Archive at Lawrence Livermore National Laboratory is supported by the Office of Science, U.S. Department of Energy. This work was partially supported by a grant from NOAA CLIVAR-Pacific.

8. References

Alexander, M.A., L. Matrosova, C. Penland, J.D. Scott, and P. Chang, 2008: Forecasting Pacific SSTs: linear inverse model predictions of the PDO. *J. Climate*, **21**, 385–402.

Battisti, D.S., and A. C. Hirst, 1989: Interannual variability in a tropical atmosphere–ocean model: Influence of the basic state, ocean geometry, and nonlinearity. *J. Atmos. Sci.,* **46,** 1687–1712.

Bergman, J.W., H.H. Hendon, and K.M. Weickmann, 2001: Intraseasonal air–sea interactions at the onset of El Niño. *J. Climate*, **14**, 1702–1719.

Bjerknes, J., 1969: Atmospheric teleconnections from the equatorial Pacific. *Mon. Wea. Rev.,* **97,** 163–172.

Borges, M. D., and P. D. Sardeshmukh, 1995: Barotropic Rossby wave dynamics of zonally varying upper level flows during northern winter. *J. Atmos. Sci.*, **52**, 3779-3796.

Burgers, G., F.-F. Jin, and G. J. van Oldenborgh, 2005: The simplest ENSO recharge oscillator. *Geophys. Res. Lett.*, **32**, L13706, doi:10.1029/2005GL022951.

Cane, M. A., and S. E. Zebiak, 1985: A theory for El Niño and the Southern Oscilation. *Science*, **228**, 1084-1087.

Chang, P., 1994: A study of seasonal cycle of sea surface temperature in the tropical Pacific ocean using reduced gravity models. *J. Geophys. Res.*, **99**, 7725-7742.

Chang, P., L. Zhang, R. Saravanan, D. J. Vimont, J. C. H. Chiang, L. Ji, H. Seidel, and M. K. Tippett, 2007: Pacific meridional mode and El Niño-Southern Oscillation. *Geophys. Res. Lett.*, **34**, L16608, doi:10.1029/2007GL030302.

Farrell, B., 1988: Optimal excitation of neutral Rossby waves. *J. Atmos. Sci.*, **45**, 163-172.

Fedorov, A.V., S.L. Harper, S.G. Philander, B. Winter, and A. Wittenberg, 2003: How Predictable is El Niño? *Bull. Amer. Meteor. Soc.*, **84**, 911–919.

Hasselmann, K., 1976: Stochastic climate models. Part I. Theory. *Tellus*, **28**, 474--485.

Hasselmann, K., 1988: PIPs and POPs: The reduction of complex dynamical systems using principal interaction and oscillation patterns. *J. Geophys. Res.*, **93**, 11015-11021.

Hendon, H. H., 2000: Impact of air-sea coupling on the MJO in a GCM. *J. Atmos. Sci.*, **57**, 3939-3952.

Hendon, H.H., M.C. Wheeler, and C. Zhang, 2007: Seasonal dependence of the MJO–ENSO relationship. *J. Climate*, **20**, 531–543.

Inness, P.M., and J.M. Slingo, 2003: Simulation of the Madden–Julian Oscillation in a coupled general circulation model. Part I: comparison with observations and an atmosphere-only GCM. *J. Climate*, **16**, 345–364.

Inness, P.M., J.M. Slingo, E. Guilyardi, and J. Cole, 2003: Simulation of the Madden–Julian Oscillation in a coupled general circulation model. Part II: The role of the basic state. *J. Climate*, **16**, 365–382.

Kessler, W.S., M. J. McPhaden, and K. M. Weickmann, 1995: Forcing of intraseasonal Kelvin waves in the equatorial Pacific. *J. Geophys. Res.*, **100**(C6), 10,613–10,631.

Kessler, W.S., 2001: EOF representations of the Madden–Julian Oscillation and its connection with ENSO. *J. Climate*, **14**, 3055–3061.

Knutson, T. R. and K. M. Weickmann, 1987: 30-60 day atmospheric oscillations: Composite life cycles of convections and circulation anomalies. *Mon. Wea. Rev.*, **115**, 1407-1436.

Jin, F.F., 1997: An equatorial ocean recharge paradigm for ENSO. Part I: Conceptual Model. *J. Atmos. Sci.*, **54**, 811–829.

Lin, J., B. Mapes, M. Zhang, and M. Newman, 2004: Stratiform precipitation, vertical heating profiles, and the Madden–Julian Oscillation. *J. Atmos. Sci.*, **61**, 296–309.

Lin, J.L., G.N. Kiladis, B.E. Mapes, K.M. Weickmann, K.R. Sperber, W. Lin, M.C. Wheeler, S.D. Schubert, A. Del Genio, L.J. Donner, S. Emori, J.F. Gueremy, F. Hourdin, P.J. Rasch, E. Roeckner, and J.F. Scinocca, 2006: Tropical intraseasonal variability in 14 IPCC AR4 climate models. Part I: Convective signals. *J. Climate*, **19**, 2665–2690.

Maloney, E. D., and D. L. Hartmann, 2001: The sensitivity in intraseasonal variability in the NCAR CCM3 to changes in convective parameterization. *J. Climate*, **14**, 2015-2034.

McPhaden, M. J., 1999: Genesis and evolution of the 1997-98 El Niño. *Science*, **283**, 950-954.

McPhaden, M. J., X. Zhang, H. H. Hendon, and M. C. Wheeler, 2006: Large scale dynamics and MJO forcing of ENSO variability. *Geophy. Res. Lett.*, **33**, L16702, doi:10.1029/2006GL026786.

Mu, M., and G. J. Zhang, 2008: Energetics of the Madden Julian oscillations in the NCAR CAM3: A composite view. *J. Geophys. Res.*, **113**, D05108, doi: 10.1029/2007JD008700.

Neelin, J. D., and F.-F. Jin, 1993: Modes of interannual tropical ocean–atmosphere interaction—A unified view. Part II: Analytical results in the weak-coupling limit. *J. Atmos. Sci.,* **50,** 3504–3522.

Neelin, J. D., and N. Zeng, 2000: A quasi-equilibrium tropical circulation model--formulation. *J. Atmos. Sci.* , **57**, 1741-1766

Newman, M., M. A. Alexander, C. R. Winkler, J. D. Scott, and J. J. Barsugli, 2000: A linear diagnosis of the coupled extratropical Ocean-Atmosphere system in the GFDL GCM. *Atmospheric Sciences Letters*, **1**, 14-25.

Newman, M., P. D. Sardeshmukh, C. R. Winkler, and J. S. Whitaker, 2003: A study of subseasonal predictability. *Mon. Wea. Rev.*, **131**, 1715-1732.

Newman, M., 2007: Interannual to decadal predictability of tropical and North Pacific sea surface temperatures. *J. Climate*, **20**, 2333-2356.

Newman, M. and P. D. Sardeshmukh, 2008: Tropical and stratospheric influences on extratropical short-term climate variability. *J. Climate*, **21**, 4326-4347.

Ortiz-Bevía, M. J., 1997: Estimation of the cyclostationary dependence in geophysical data fields. *J. Geophys. Res.*, **102**, 13,473-13,486.

Papanicolaou, G. and W. Kohler, 1974: Asymptotic theory of mixing stochastic ordinary differential equations. *Commun. Pure Appl. Math.*, **27**, 641-668.

Pegion, K., and B. P. Kirtman, 2008: The impact of air-sea interactions in the simulation of tropical intraseasonal variability. *J. Climate*, submitted.

Penland, C., 1989: Random forcing and forecasting using principal oscillation pattern analysis. *Mon. Wea. Rev.*, **117**, 2165—2185.

Penland, C., 1996: A stochastic model of IndoPacific sea surface temperature anomalies. *Physica D*, **98**, 534--558.

Penland, C., and L. Matrosova, 1994: A balance condition for stochastic numerical models with application to the El Niño-Southern Oscillation. *J. Climate*, **7**, 1352-1372.

Penland, C., and P. D. Sardeshmukh, 1995: The optimal growth of tropical sea surface temperature anomalies. *J. Climate*, **8**, 1999—2024.

Pohl, B., and A.J. Matthews, 2007: observed changes in the lifetime and amplitude of the Madden–Julian Oscillation associated with interannual enso sea surface temperature anomalies. *J. Climate*, **20**, 2659–2674.

Reynolds, R.W., N.A. Rayner, T.M. Smith, D.C. Stokes, and W. Wang, 2002: An improved in situ and satellite SST analysis for climate. *J. Climate*, **15**, 1609–1625.

Roundy, P.E., and G.N. Kiladis, 2006: Observed relationships between oceanic Kelvin waves and atmospheric forcing. *J. Climate*, **19**, 5253–5272.

Sardeshmukh, P. D., and B. J. Hoskins, 1984: Spatial smoothing on the sphere. *Mon. Wea. Rev.*, **112**, 2524—2529.

Sardeshmukh, P. D., 1993: The baroclinic chi problem and its application to the diagnosis of atmospheric heating rates. *J. Atmos. Sci.*, **50**, 1099—1112.

Sardeshmukh, P. D., M. Newman, and C. R. Winkler, 1999: Dynamically consistent estimates of diabatic heating. Proceedings, 24th Annual Climate Diagnostics and Prediction Workshop, Tucson, AZ, 172--175.

Sardeshmukh, P. D., G. P. Compo, and C. Penland, 2000: Changes of probability associated with El Niño. *J. Climate*, **13**, 4268-4286.

Schopf, P. S., and M. J. Suarez, 1988: Vacillations in a coupled ocean–atmosphere model. *J. Atmos. Sci.,* **45,** 549–566.

Shinoda, T., H. H. Hendon, and J. Glick, 1998: Intraseasonal variability of surface fluxes and sea surface temperature in the tropical western Pacific and Indian oceans. *J. Climate*, **11**, 1685-1702.

Sperber, K. R., S. Gualdi, S. Legutke, and V. Gayler, 2005: The Madden-Julian oscillation in ECHAM4 coupled and uncoupled GCMs. *Clim. Dyn.*, **25**, 117-140.

Tam, C.-Y., and N.-C. Lau, 2005: Modulation of the Madden-Julian oscillation by ENSO: Inferences from observations and GCM simulations. *J. Met. Soc. Japan*, **83**, 727-743.

Thompson, C.J., and D.S. Battisti, 2000: A linear stochastic dynamical model of ENSO. Part I: Model Development. *J. Climate*, **13**, 2818–2832.

van Oldenborgh, G.J., 2000: What caused the onset of the 1997–98 El Niño? *Mon. Wea. Rev.*, **128**, 2601–2607.

Vimont, D.J., J.M. Wallace, and D.S. Battisti, 2003: The seasonal footprinting mechanism in the Pacific: Implications for ENSO. *J. Climate*, **16**, 2668–2675.

Vitart, F., S. Woolnough, M.A. Balmaseda, and A.M. Tompkins, 2007: Monthly forecast of the Madden–Julian Oscillation using a coupled GCM. *Mon. Wea. Rev.*, **135**, 2700–2715.

von Storch, H., T. Bruns, I. Fischer-Bruns, and K. Hasselmann, 1988: Principal Oscillation Pattern analysis of the 30–60 day oscillation in a GCM equatorial troposphere. *J. Geophys. Res.*, **93**, 11022–11036.

Waliser, D., et al., 2008: MJO simulation diagnostics. *J. Climate*, submitted.

Wang, C., R.H. Weisberg, and H. Yang, 1999: Effects of the wind speed–evaporation–SST feedback on the El Niño–Southern Oscillation. *J. Atmos. Sci.*, **56**, 1391–1403.

Wheeler, M.C., and H.H. Hendon, 2004: An all-season real-time multivariate MJO index: Development of an index for monitoring and prediction. *Mon. Wea. Rev.*, **132**, 1917–1932.

Winkler, C. R., M. Newman, and P. D. Sardeshmukh, 2001: A linear model of wintertime low-frequency variability. Part I: Formulation and forecast skill. *J. Climate*, **14**, 4474-4494.

Woolnough, S.J., J.M. Slingo, and B.J. Hoskins, 2000: The relationship between convection and sea surface temperature on intraseasonal timescales. *J. Climate*, **13**, 2086–2104.

Wu, R., B. P. Kirtman, and K. Pegion, 2006: Local air-sea relationship in observations and model simulations. *J. Climate*, **19**, 4914-4932.

Zavala-Garay, J., C. Zhang, A.M. Moore, and R. Kleeman, 2005: The linear response of ENSO to the Madden–Julian Oscillation. *J. Climate*, **18**, 2441–2459.

Zhang, C., 2001: Intraseasonal perturbations in sea surface temperatures of the equatorial eastern pacific and their association with the Madden–Julian oscillation. *J. Climate*, **14**, 1309–1322.

Zhang, C., and J. Gottschalck, 2002: SST anomalies of ENSO and the Madden–Julian Oscillation in the equatorial Pacific. *J. Climate*, **15**, 2429–2445.

Zhang, C., M. Dong, S. Gualdi, H. H. Hendon, E. D. Maloney, A. Marshall, K. R. Sperber, and W. Wang, 2006: Simulations of the Madden-Julian oscillation in four pairs of coupled and uncoupled global models. *Clim. Dyn.*, **27**, 573-592.

Zhang, G.J., and M. Mu, 2005: Simulation of the Madden–Julian Oscillation in the NCAR CCM3 using a revised Zhang–McFarlane convection parameterization scheme. *J. Climate*, **18**, 4046–4064.

Zheng, Y., D.E. Waliser, W.F. Stern, and C. Jones, 2004: The role of coupled sea surface temperatures in the simulation of the tropical intraseasonal oscillation. *J. Climate*, **17**, 4109–4134.

9. Figures

Figure 1: Spectra of the leading principal component (PC) of monthly tropical SST variability from observations (pink line) compared to spectra derived from the output of the C-LIM (blue line) and the "20th-century" (20c3m) IPCC AR4 coupled GCMs (thin black, yellow, blue, and green lines). The observed spectrum was computed from the time series of the leading PC as determined from an EOF analysis of monthly SST anomalies in the region between 25°S-25°N for the years 1950-1999. The C-LIM was constructed as described in the paper from weekly 1982-2005 data, and then a 100-member ensemble of 50-yr LIM model runs was made. For consistent comparison and because it is the real system these sophisticated models are trying to simulate, both LIM and GCM model output were projected onto the leading observed EOF of monthly anomalous SST to produce PC time series in each model, for the same 1950-1999 period. Gray shading indicates the 95% confidence interval from the LIM, based on the spread of the 100 ensemble members (see paper for more details).

Figure 2: Total variance (contours) and fraction of local variance explained by EOF truncation (gray shading) for selected variables used in the model. Top: SST ($\mathbf{T}_O$); contour inteval 0.25 K^2. 2nd row: 850 hPa streamfunction (ψ_{250}); contour interval 2.5 x 10^{12} m^4/s^2. 3rd row: diabatic heating ($\mathbf{H}_{400}$); contour interval 7.5 x 10^{-11} K^2/s^2. Bottom row: 250 hPa velocity potential (χ_{250}); contour interval 1.5 x 10^{12} m^4/s^2. Thicker contours

indicate larger values, starting at 1 K^2, 1 x 10^{13} m^4/s^2, 30 x 10^{-11} K^2/s^2, and 9 x 10^{12} m^4/s^2, respectively.

Figure 3: Selected highpass filtered fields linearly regressed on the two leading highpass PCs. $\mathbf{T}_O$ is indicated by shading (contour interval 0.0075 K), $\mathbf{H}_{400}$ by contours (contour interval 1.2 x 10^{-6} K/s), and 850 hPa winds (derived from ψ_{850} and χ_{850}) by the black vectors, with wind speeds below 0.125 m/s removed for clarity.

Figure 4. Forecast skill of $\mathbf{H}_{400}$ for forecast leads of 28 and 150 days, for (a and b) the C-LIM, (c and d) the A-LIM, and (e and f) the C-LIM with only atmospheric initial conditions. Contour interval is 0.1.

Figure 5. Forecast skill of $\mathbf{T}_O$ for forecast leads of 150 and 270 days, for (a and b) the C-LIM, (c and d) the O-LIM, and (e and f) the C-LIM with only SST initial conditions.

Figure 6. Observed (left panels) and LIM (right panels) lag-covariance. (a-b): 28-day lag-covariance of $\mathbf{H}_{400}$ (contour interval=2.5 x 10^{-11} K^2/s^2). (c-d): 150-day lag-covariance of $\mathbf{T}_O$ (contour interval=0.125 K^2). (e-f): 270-day lag-covariance of $\mathbf{T}_O$ (contour interval=0.125 K^2).

Figure 7. Power spectra for the three leading SST ($\mathbf{T}_O$) PCs (red lines), compared to that predicted by the LIM (blue lines). Gray shading represents the 95% confidence interval determined from a 2400 yr run of the LIM (see text for further details). The green lines indicate spectra generated by the "uncoupled" version of the LIM (i.e., $\mathbf{L}_{OA}$=$\mathbf{L}_{AO}$). In these log(frequency) versus power times angular frequency (ω) plots, the area under any portion of the curve is equal to the variance within that frequency band. Note that

displaying power times frequency slightly shifts the power spectral density peak centered at a period of 4.5 years to a variance peak centered at a period of 3.5 years. Insets in each panel show the corresponding EOF and the variance explained by that pattern.

Figure 8. Same as Fig. 7 but for the three leading diabatic heating (**H**) PCs. In addition, the dashed lines represent the spectra of the observed heating PCs projected onto the subset of either the "coupled" (yellow) or "internal" (pink) eigenmodes of the full operator.

Figure 9. Comparison of the full and uncoupled operators. a) frequency vs. eft of each eigenvalues from the full (circle) and uncoupled (cross) operators, where the eigenvalues corresponding to the "coupled" and "SST-only" modes are blue, and the "internal atmosphere" and "atmosphere-only" modes are red. b) Maximum pattern correlation between the corresponding eigenmodes of the full and uncoupled operators.

Figure 10. SST ($\mathbf{T}_O$) portion of the two leading empirical propagating eigenmodes from the full ($\mathbf{L}$) and uncoupled ($\mathbf{L}_{unc}$) operators. (a-b) Leading propagating (and least damped overall) eigenmode of $\mathbf{L}$. (a) cos phase, (b) sin phase. (c-d) Leading propagating (and second least damped overall) eigenmode of $\mathbf{L}_{unc}$. (c) cos phase, (d) sin phase. Contour interval is the same in all panels but is arbitrary. The overall sign of each panel is also arbitrary; within each panel, values of one sign are depicted with gray shading and thick contours, and the other sign with thin contours.

Figure 11. 400 hPa diabatic heating (**H**) portion of the "MJO" eigenmode, which is the leading (least damped) "internal atmospheric" eigenmode of $\mathbf{L}$ and the leading "atmosphere-only" eigenmode of $\mathbf{L}_{unc}$. For each eigenmode, left panels show the cos

phase and right panels show the sin phase. Contour interval is the same in all panels but is arbitrary. The overall sign of each panel is also arbitrary; within each panel, values of one sign are depicted with gray shading and thick contours, and the other sign with thin contours.

Figure 12. Evolution of "MJO" initial condition by the C-LIM dynamical operator **L** and by the uncoupled version of the C-LIM ($\mathbf{L}_{unc}$). a) Initial $\mathbf{T}_O$ and $\mathbf{H}_{400}$ state, obtained from the regression of the highpass data against highpass PC1 (Fig. 3a), and b) the full evolved state 13 days later. $\mathbf{T}_O$ is indicated by shading (contour interval 0.0075 K) and $\mathbf{H}_{400}$ by contours (contour interval 1.2 x 10^{-6} K/s). 850 hPa winds (derived from ψ_{850} and χ_{850}) are indicated by the black vectors, with wind speeds below 0.125 m/s removed for clarity. c) Hovmuller diagram of the full C-LIM evolution of $\mathbf{T}_O$ (shading; contour interval 0.0075 K) and $\mathbf{H}_{400}$ (contours; contour interval 1.2 x 10^{-6} K/s) averaged between 2^0S-2^0N. d) Hovmuller diagram of the full C-LIM evolution of χ_{850} (shading; contour interval 1.75 x 10^6 m^2/s) and ψ_{850} (contours; contour interval 1.75 x 10^6 m^2/s) at 8^0N. e and f) Same as c) and d) but for the uncoupled C-LIM simulation starting with the same initial conditions. Note that for this linear model, sign in all panels is arbitrary, but that to match the direction of the wind vectors the black contours and yellow/red shading are positive, and red contours and blue shading are negative.

Figure 13. Evolution of the optimal initial condition for amplification of SST anomalies over a 150-day interval. a) Initial $\mathbf{T}_O$ and $\mathbf{H}_{400}$ state, and the evolved states b) 15 and c) 150 days later. $\mathbf{T}_O$ is indicated by shading (contour interval 0.075 K) and $\mathbf{H}_{400}$ by contours (contour interval 1.2 x 10^{-6} K/s). 850 hPa winds (derived from ψ_{850} and χ_{850}) are

indicated by the black vectors, with wind speeds below 0.125 m/s removed for clarity. In panel a, all wind (heating) anomalies fall below the minimum vector (contour) value and so do not appear. d) Hovmuller diagram of the C-LIM evolution of $\mathbf{T}_O$ (shading; contour interval 0.075 K) and $\mathbf{H}_{400}$ (contours; contour interval 1.2 x 10^{-6} K/s) at the equator. e) Hovmuller diagram of the C-LIM evolution of χ_{850} (shading; contour interval 1.75 x 10^6 m^2/s) and ψ_{850} (contours; contour interval 1.75 x 10^6 m^2/s) at 8^0N. f) Same as Fig. 13d except for the coupled mode component $\mathbf{x}^{coup}$ only. Note that for this linear model, sign in all panels is arbitrary, but that to match the direction of the wind vectors the black contours and yellow/red shading are positive, and red contours and blue shading are negative. Amplitudes are also arbitrary, but are scaled to have representative values; note that contour intervals for the atmospheric variables are as in Fig. 12 but are a factor of ten larger for $\mathbf{T}_O$.

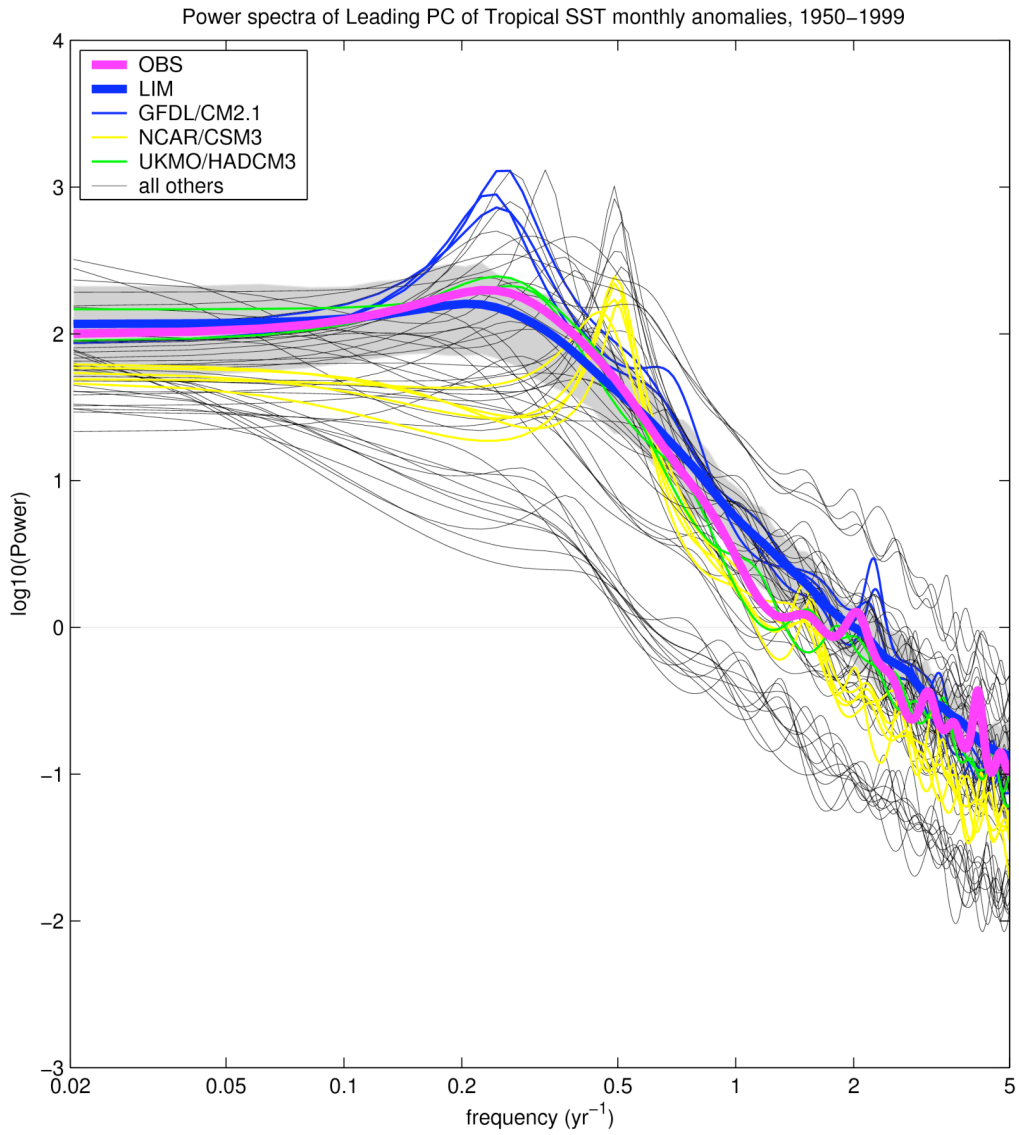

Figure 1: Spectra of the leading principal component (PC) of monthly tropical SST variability from observations (pink line) compared to spectra derived from the output of the C-LIM (blue line) and the "20th-century" (20c3m) IPCC AR4 coupled GCMs (thin black, yellow, blue, and green lines). The observed spectrum was computed from the time series of the leading PC as determined from an EOF analysis of monthly SST anomalies in the region between 25°S-25°N for the years 1950-1999. The C-LIM was constructed as described in the paper from weekly 1982-2005 data, and then a 100-member ensemble of 50-yr LIM model runs was made. For consistent comparison and because it is the real system these sophisticated models are trying to simulate, both LIM and GCM model output were projected onto the leading observed EOF of monthly anomalous SST to produce PC time series in each model, for the same 1950-1999 period. Gray shading indicates the 95% confidence interval from the LIM, based on the spread of the 100 ensemble members (see paper for more details).

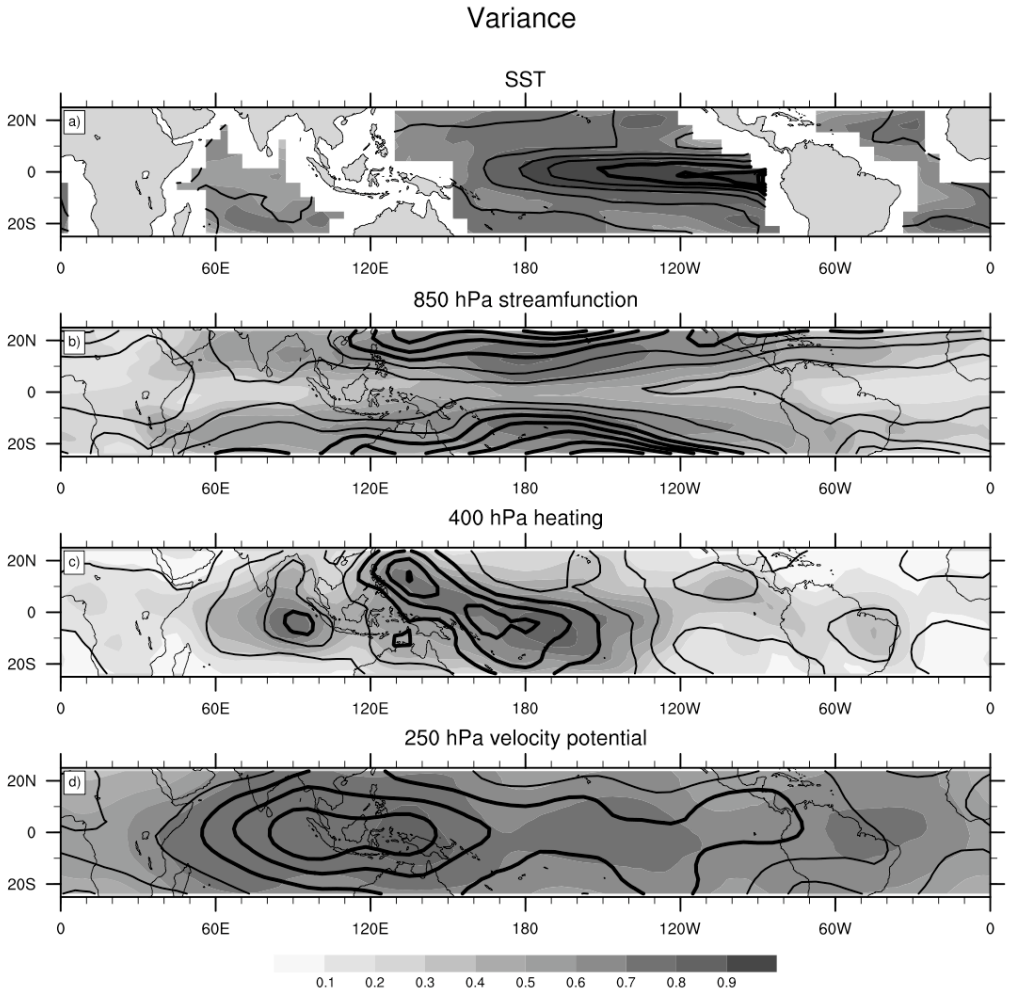

Figure 2: Total variance (contours) and fraction of local variance explained by EOF truncation (gray shading) for selected variables used in the model. Top: SST ($\mathbf{T}_O$); contour inteval 0.25 K^2. 2nd row: 850 hPa streamfunction ($\boldsymbol{\psi}_{250}$); contour interval 2.5 x 10^{12} m^4/s^2. 3rd row: diabatic heating ($\mathbf{H}_{400}$); contour interval 7.5 x 10^{-11} K^2/s^2. Bottom row: 250 hPa velocity potential ($\boldsymbol{\chi}_{250}$); contour interval 1.5 x 10^{12} m^4/s^2. Thicker contours indicate larger values, starting at 1 K^2, 1 x 10^{13} m^4/s^2, 30 x 10^{-11} K^2/s^2, and 9 x 10^{12} m^4/s^2, respectively.

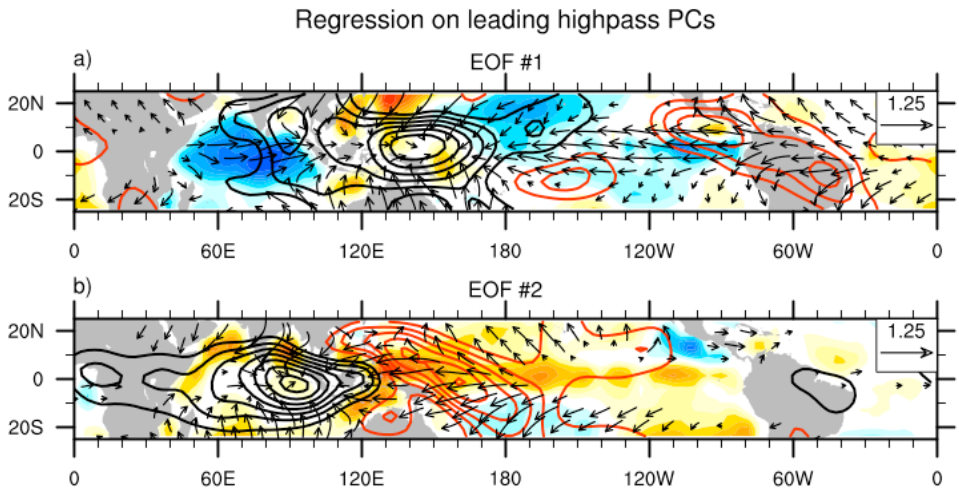

Figure 3: Selected highpass filtered fields linearly regressed on the two leading highpass PCs. $\mathbf{T}_O$ is indicated by shading (contour interval 0.0075 K), $\mathbf{H}_{400}$ by contours (contour interval 1.2 x 10^{-6} K/s), and 850 hPa winds (derived from ψ_{850} and χ_{850}) by the black vectors, with wind speeds below 0.125 m/s removed for clarity.

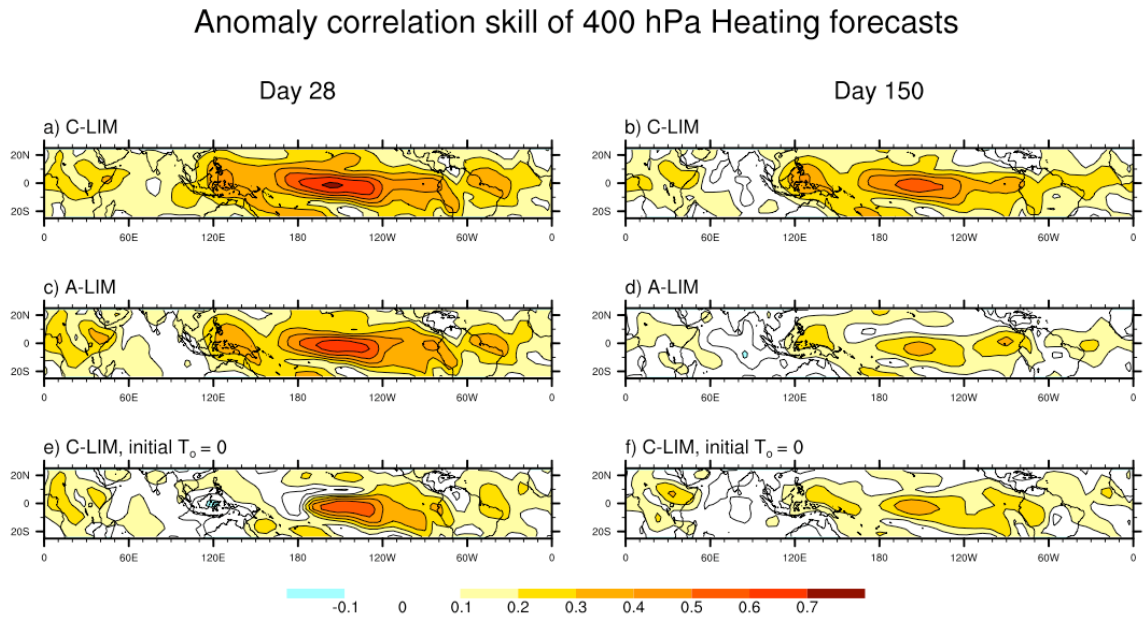

Figure 4. Forecast skill of $\mathbf{H}_{400}$ for forecast leads of 28 and 150 days, for (a and b) the C-LIM, (c and d) the A-LIM, and (e and f) the C-LIM with only atmospheric initial conditions. Contour interval is 0.1.

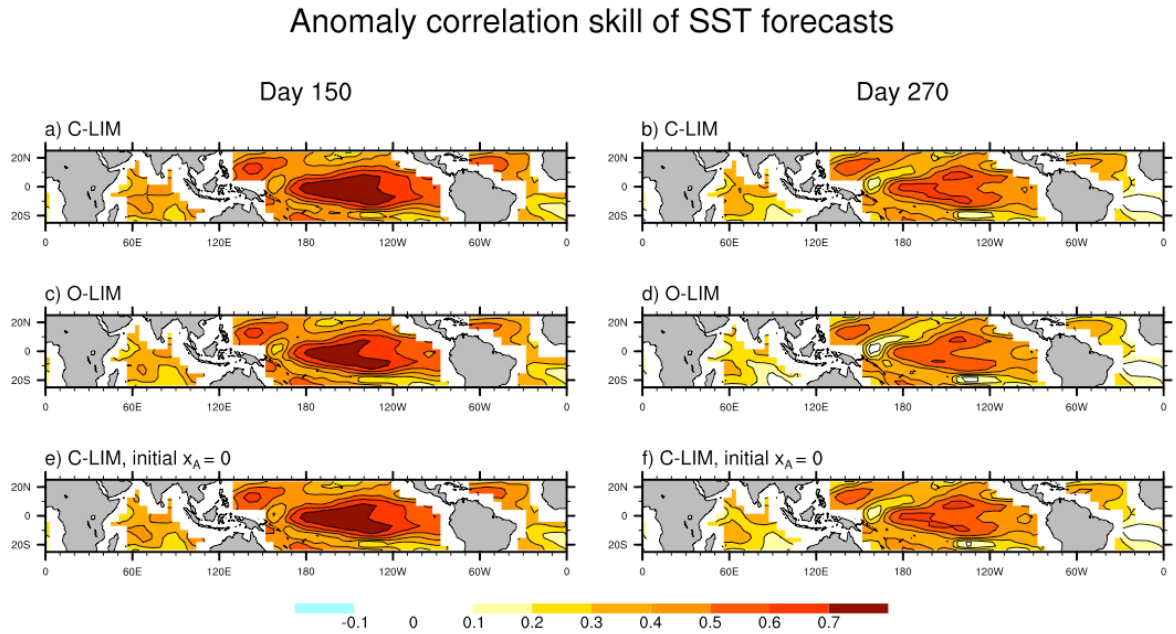

Figure 5. Forecast skill of $\mathbf{T}_O$ for forecast leads of 150 and 270 days, for (a and b) the C-LIM, (c and d) the O-LIM, and (e and f) the C-LIM with only SST initial conditions. Contour interval is 0.1.

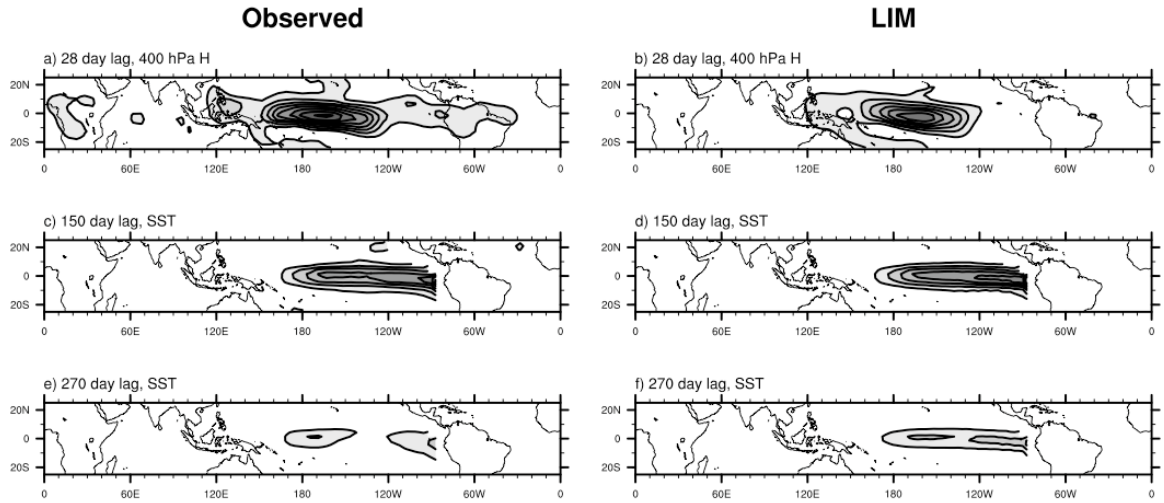

Figure 6. Observed (left panels) and LIM predicted (right panels) lag-covariance. (a-b): 28-day lag-covariance of $\mathbf{H}_{400}$ (contour interval=2.5 x 10^{-11} K^2/s^2). (c-d): 150-day lag-covariance of $\mathbf{T}_O$ (contour interval=0.125 K^2). (e-f): 270-day lag-covariance of $\mathbf{T}_O$ (contour interval=0.125 K^2).

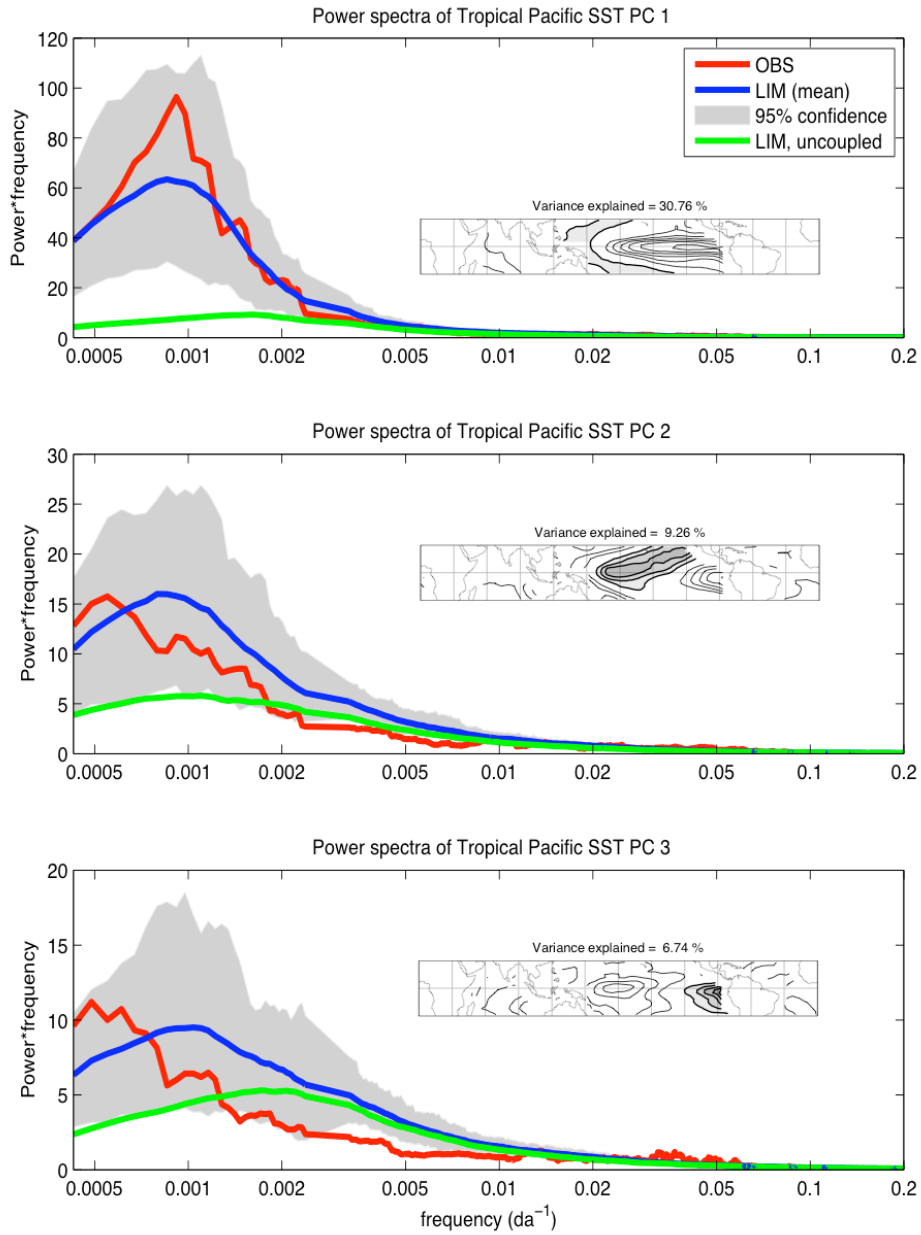

Figure 7. Power spectra for the three leading SST ($\mathbf{T}_O$) PCs (red lines), compared to that predicted by the LIM (blue lines). Gray shading represents the 95% confidence interval determined from a 2400 yr run of the LIM (see text for further details). The green lines indicate spectra generated by the "uncoupled" version of the LIM ($\mathbf{L}_{un}$). In these log(frequency) versus power times angular frequency (ω) plots, the area under any portion of the curve is equal to the variance within that frequency band. Note that displaying power times frequency slightly shifts the power spectral density peak centered at a period of 4.5 years to a variance peak centered at a period of 3.5 years. Insets in each panel show the corresponding EOF and the variance explained by that pattern.

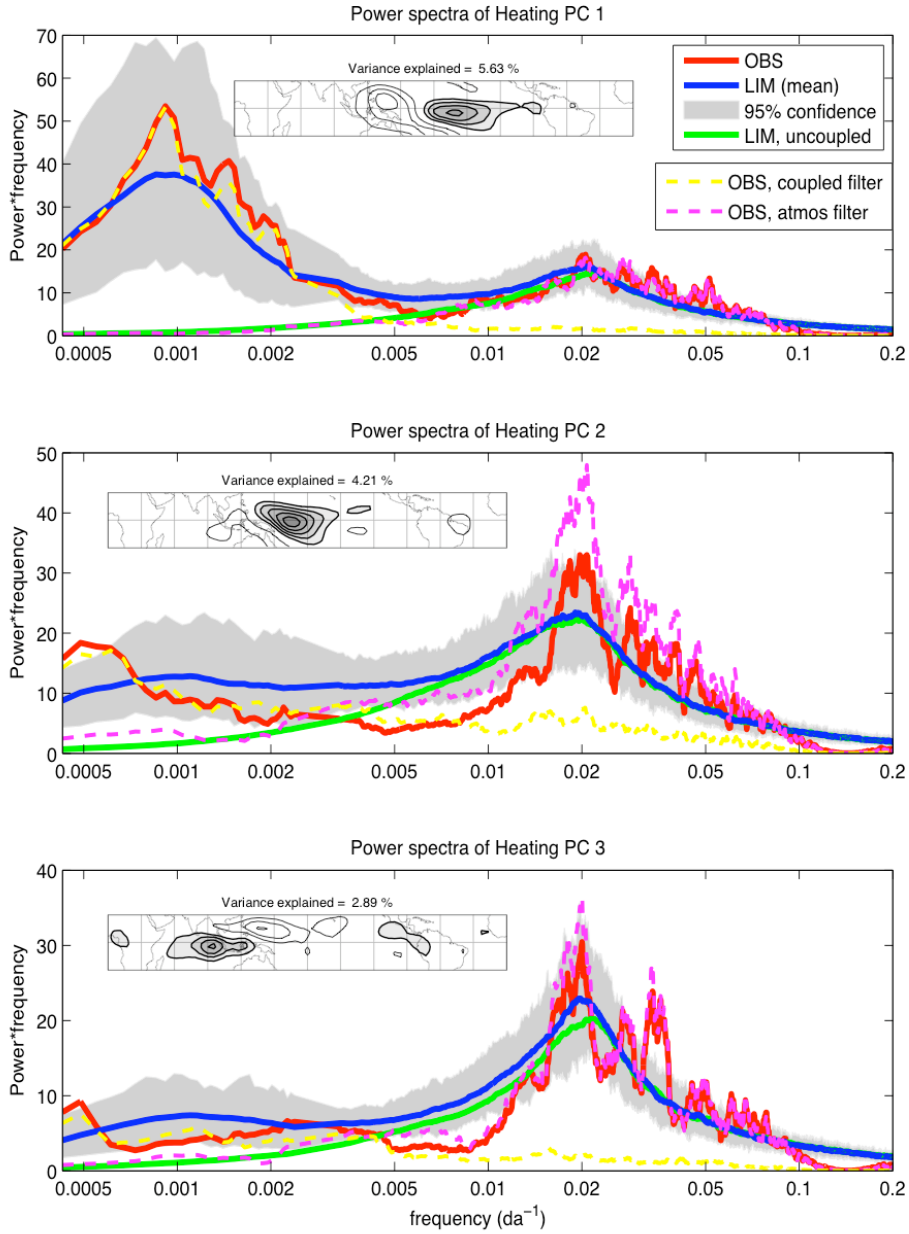

Figure 8. Same as Fig. 7 but for the three leading diabatic heating (**H**) PCs. In addition, the dashed lines represent the spectra of the observed heating PCs projected onto the subset of either the "coupled" (yellow) or "internal" (pink) eigenmodes of the full operator.

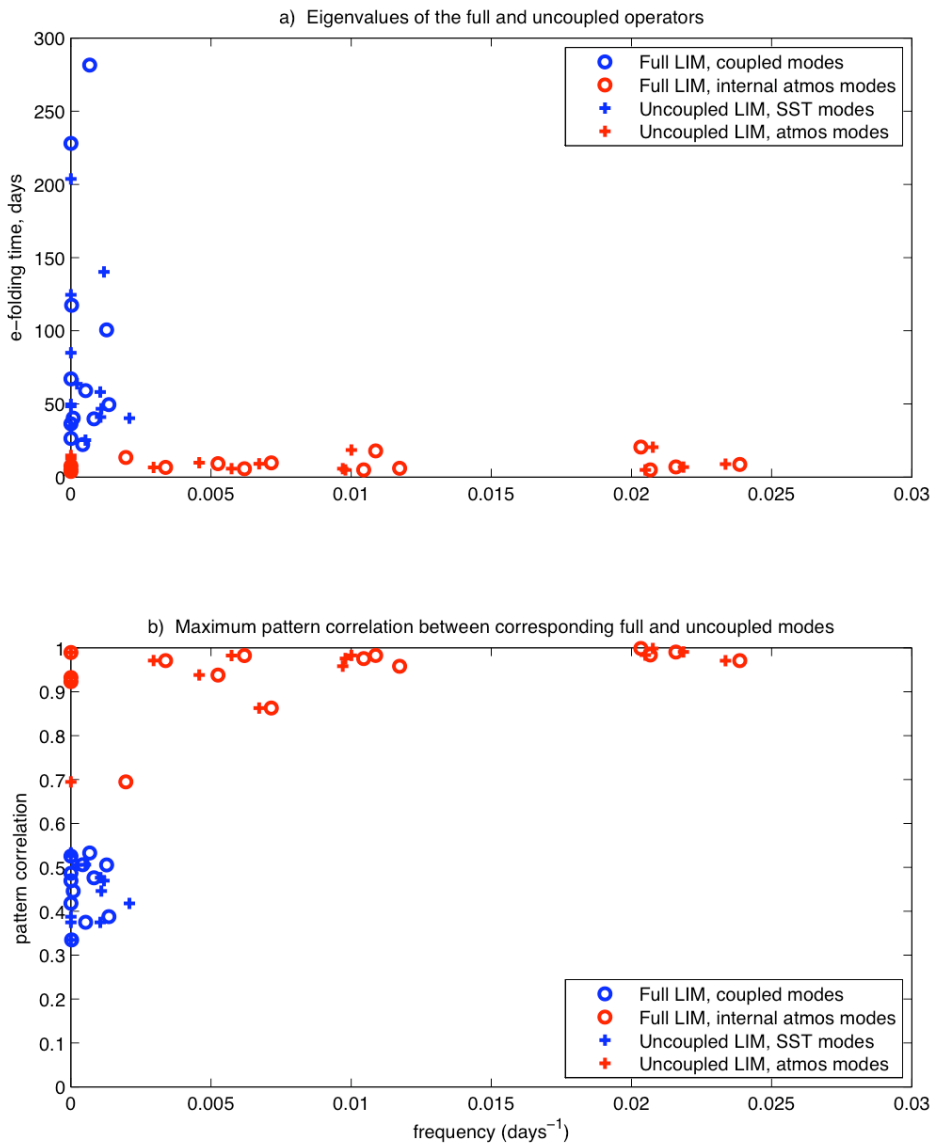

Figure 9. Comparison of the full and uncoupled operators. a) frequency vs. eft of each eigenvalue from the full (circle) and uncoupled (cross) operators, where the eigenvalues corresponding to the "coupled" and "SST-only" modes are blue, and the "internal atmospheric" and "atmosphere-only" modes are red. b) Maximum pattern correlation between the corresponding eigenmodes of the full and uncoupled operators.

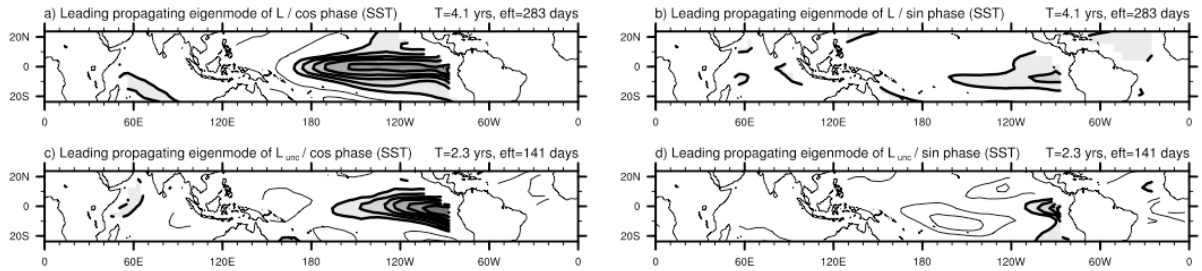

Figure 10. SST ($\mathbf{T}_O$) portion of the the leading empirical propagating eigenmodes from the full ($\mathbf{L}$) and uncoupled ($\mathbf{L}_{unc}$) operators. (a-b) Leading propagating (and least damped overall) eigenmode of $\mathbf{L}$. (a) cos phase, (b) sin phase. (c-d) Leading propagating (and second least damped overall) eigenmode of $\mathbf{L}_{unc}$. (c) cos phase, (d) sin phase. Contour interval is the same in all panels but is arbitrary. The overall sign of each panel is also arbitrary; within each panel, values of one sign are depicted with gray shading and thick contours, and the other sign with thin contours.

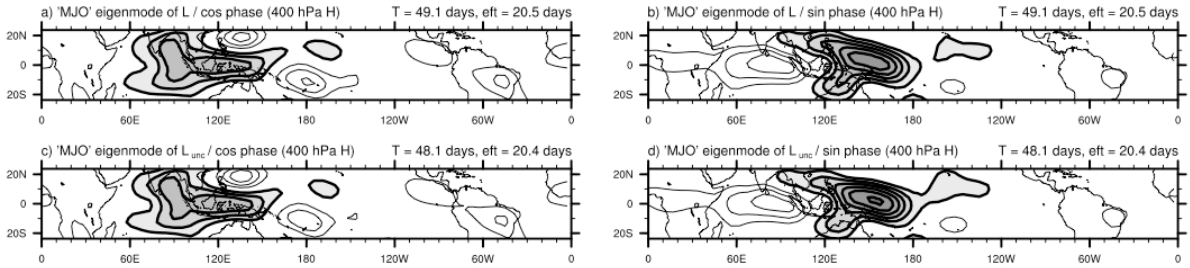

Figure 11. 400 hPa diabatic heating (**H**) portion of the "MJO" eigenmode, which is the leading (least damped) "internal atmospheric" eigenmode of **L** and the leading "atmosphere-only" eigenmode of $\mathbf{L}_{unc}$. For each eigenmode, left panels show the cos phase and right panels show the sin phase. Contour interval is the same in all panels but is arbitrary. The overall sign of each panel is also arbitrary; within each panel, values of one sign are depicted with gray shading and thick contours, and the other sign with thin contours.

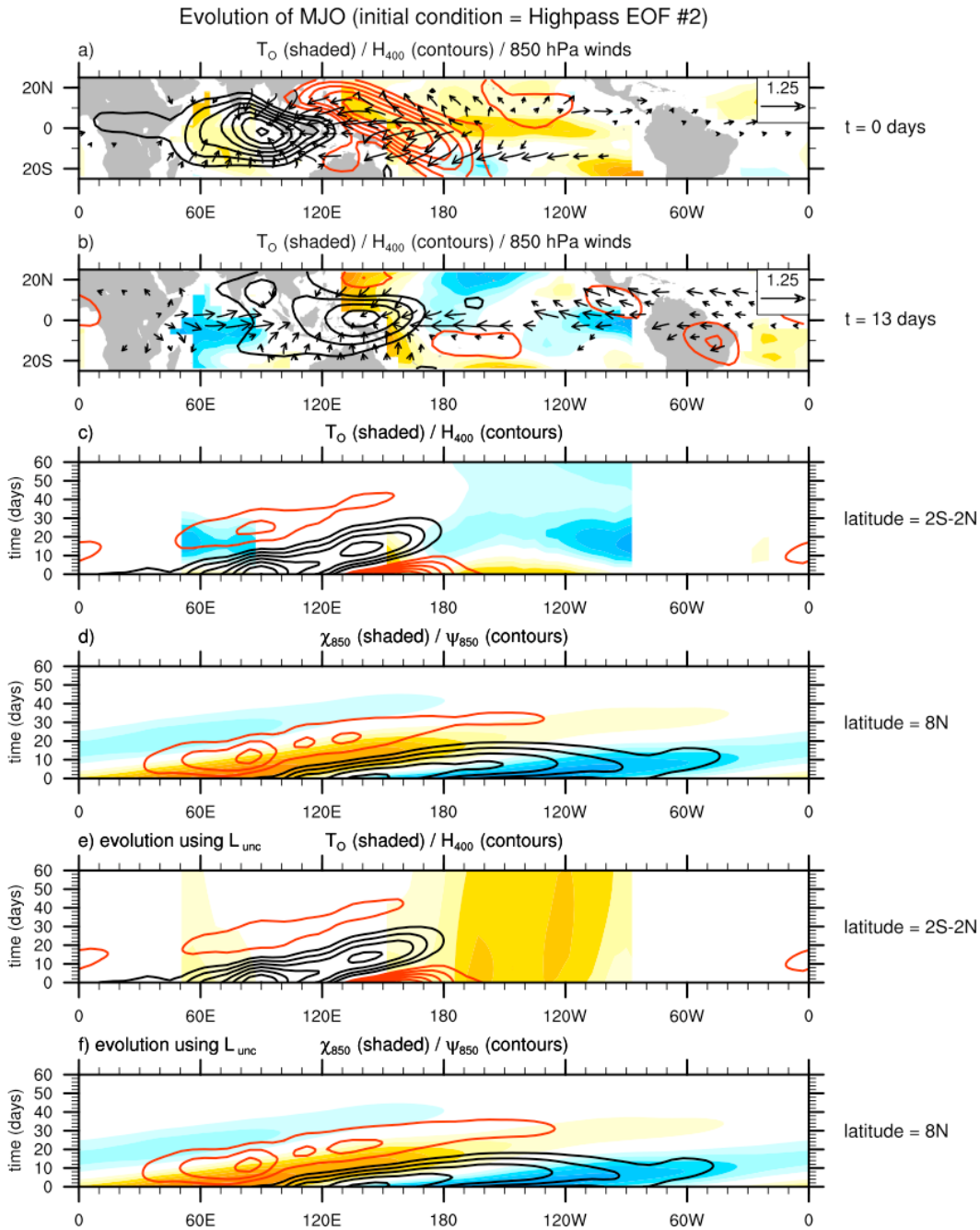

Figure 12. Evolution of "MJO" initial condition by the C-LIM dynamical operator **L** and by the uncoupled version of the C-LIM ($\mathbf{L}_{unc}$). a) Initial $\mathbf{T}_O$ and $\mathbf{H}_{400}$ state, obtained from the regression of the highpass data against highpass PC1 (Fig. 3a), and b) the full evolved state 13 days later. $\mathbf{T}_O$ is indicated by shading (contour interval 0.0075 K) and $\mathbf{H}_{400}$ by contours (contour interval 1.2 x 10^{-6} K/s). 850 hPa winds (derived from ψ_{850} and χ_{850}) are indicated by the black vectors, with wind speeds below 0.125 m/s removed for clarity. c) Hovmuller diagram of the full C-LIM evolution of $\mathbf{T}_O$ (shading; contour interval 0.0075 K) and $\mathbf{H}_{400}$ (contours; contour interval 1.2 x 10^{-6} K/s) averaged between 2^0S-2^0N. d) Hovmuller diagram of the full C-LIM evolution of χ_{850} (shading; contour interval 1.75 x 10^6 m^2/s) and ψ_{850} (contours; contour interval 1.75 x 10^6 m^2/s) at 8^0N. e and f) Same as c) and d) but for the uncoupled C-LIM simulation starting with the same initial conditions. Note that for this linear model, sign in all panels is arbitrary, but that to match the direction of the wind vectors the black contours and yellow/red shading are positive, and red contours and blue shading are negative.

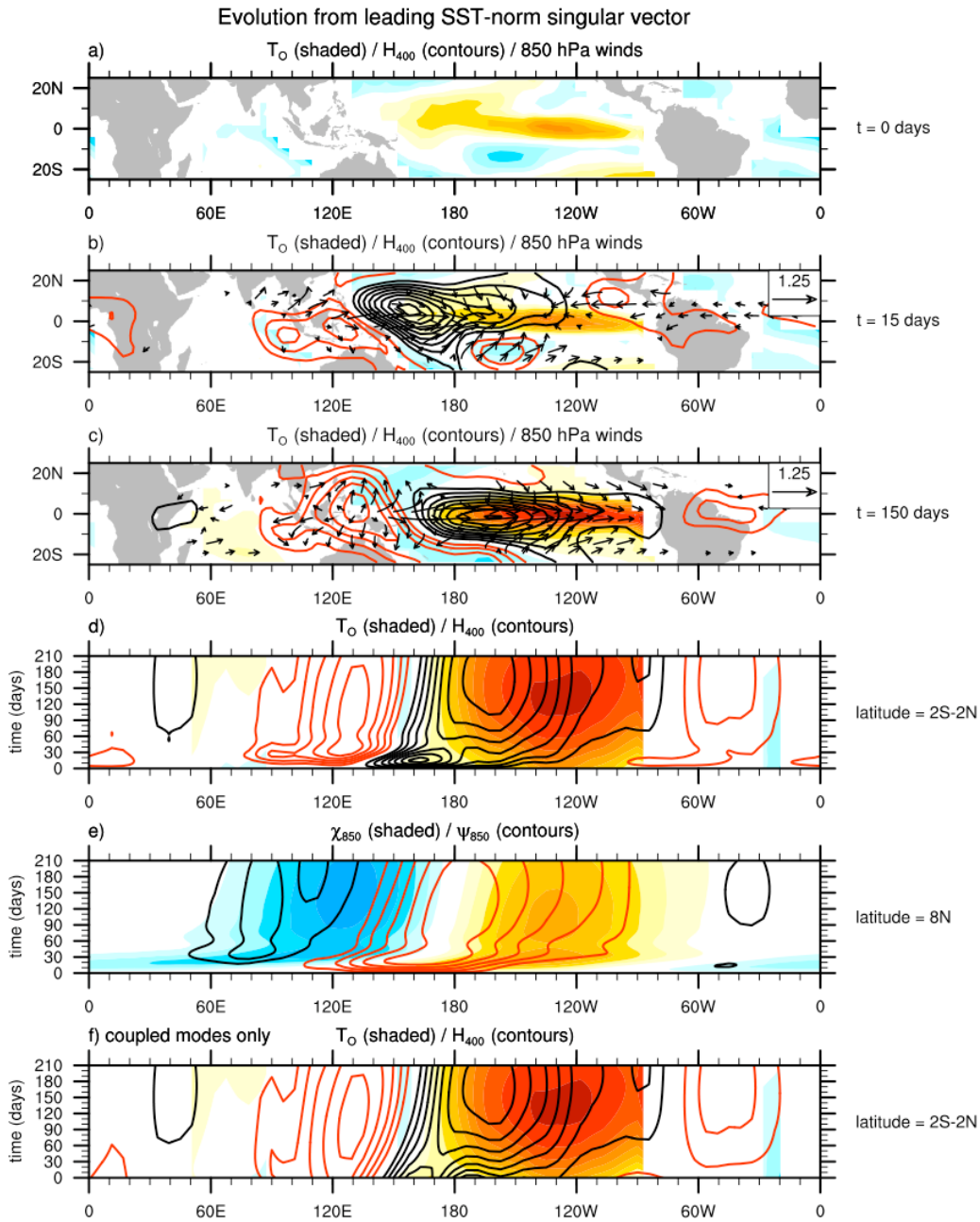

Figure 13. Evolution of the optimal initial condition for amplification of SST anomalies over a 150-day interval. a) Initial $\mathbf{T}_O$ and $\mathbf{H}_{400}$ state, and the evolved states b) 15 and c) 150 days later. $\mathbf{T}_O$ is indicated by shading (contour interval 0.075 K) and $\mathbf{H}_{400}$ by contours (contour interval 1.2 x 10^{-6} K/s). 850 hPa winds (derived from ψ_{850} and χ_{850}) are indicated by the black vectors, with wind speeds below 0.125 m/s removed for clarity. In panel a, all wind (heating) anomalies fall below the minimum vector (contour) value and so do not appear. d) Hovmuller diagram of the C-LIM evolution of $\mathbf{T}_O$ (shading; contour interval 0.075 K) and $\mathbf{H}_{400}$ (contours; contour interval 1.2 x 10^{-6} K/s) averaged between 2^0S-2^0N. e) Hovmuller diagram of the C-LIM evolution of χ_{850} (shading; contour interval 1.75 x 10^6 m^2/s) and ψ_{850} (contours; contour interval 1.75 x 10^6 m^2/s) at 8^0N. f) Same as Fig. 13d except for the coupled mode component $\mathbf{x}^{coup}$ only. Note that for this linear model, sign in all panels is arbitrary, but that to match the direction of the wind vectors the black contours and yellow/red shading are positive, and red contours and blue shading are negative. Amplitudes are also arbitrary, but are scaled to have representative values; note that contour intervals for the atmospheric variables are as in Fig. 12 but are a factor of ten larger for $\mathbf{T}_O$.